Electronic and heat transport phenomena in the nanogranular thiospinel Fe₃S₄

Karel Knížek [1,*] Miroslav Soroka [1,2,3] Ondřej Kaman,[1] Jarmila Kuličková [1] Petr Levinský,[1]
Jiří Hejtmánek [1] and Zdeněk Jirák [1]

[1]*Institute of Physics of the Czech Academy of Sciences, 162 00 Prague 6, Czech Republic*
[2]*Institute of Inorganic Chemistry of the Czech Academy of Sciences, 250 68 Rez, Czech Republic*
[3]*Charles University, Faculty of Science, 128 43 Prague 2, Czech Republic*

The iron sulphide Fe₃S₄ (greigite) is similar to its oxide counterpart Fe₃O₄ (magnetite) as to the crystal structure and ferrimagnetic order, but differs in electronic states. The *ab initio* calculations have evidenced *p*-type carriers at three spin-minority and three spin-majority Fermi surfaces, which is in contrast to the half-metallic character of magnetite with *n*-type carriers at three spin-minority Fermi surfaces. The transport properties including Hall and Nernst effects have been studied over the range 2–300 K by using nanogranular ceramics prepared by cold isostatic pressing of Fe₃S₄ particles with the mean crystallite size of $d_{XRD} \approx 80$ and 30 nm, respectively. The samples show metalliclike electrical resistivity with large residual value at $T \to 0$ K. The *p*-type character of the charge carriers is reflected by the positive sign of both the thermopower and Hall effect. Temperature dependencies of the electrical resistivity, thermal conductivity, and thermopower are analyzed by considering processes of the grain boundary and defect intragrain scattering; simultaneously the role of magnons and their dynamics in electronic and heat transport is revealed. The Nernst and Hall effects show dominant contributions of anomalous type (ANE and AHE) with signs exactly opposite to those of Fe₃O₄, i.e., positive AHE and negative ANE in Fe₃S₄. The results are interpreted by evoking the original Callen treatment of thermoelectric and thermomagnetic phenomena using Onsager equations. Scaling between the longitudinal and transverse components of the electrical resistivity and thermoelectric conductivity tensors is checked. The analysis of the temperature dependent AHE using the relation between transverse and longitudinal resistivity $\rho_{yx}^A(T) \sim \rho_{xx}(T)^n$ gives the characteristic exponent $n = 1.15$, which is close to the $n = 1$ predicted by the skew-scattering mechanism.

I. INTRODUCTION

The thiospinel Fe₃S₄ known under the mineral name greigite is naturally occurring in a form of tiny crystallites in sedimentary rocks, whose origin is usually related to magnetotactic and sulfate-reducing bacteria [1,2]. Although several methods for the synthesis of greigite have been described, the main obstacle to prepare pure-phase samples is the metastable nature of greigite. When heated in air at temperatures above 200 °C, Fe₃S₄ is converted to a mixture of pyrrhotite (Fe₁₋ₓS) and either pyrite (cubic FeS₂) or sulphur, and finally is oxidized to Fe₃O₄ and maghemite (γ-Fe₂O₃); see, e.g., [3]. Hydrothermal methods, which are typically carried out at low temperatures (<300 °C) under autogeneous pressure of water, have appeared especially suitable for obtaining almost pure greigite. In particular, Chang and co-workers [4,5] synthesized highly pure and well-crystallized greigite with the grain size up to 44 μm by reacting FeCl₃ with H₂S generated from thiourea in the presence of formic acid at 170 °C under hydrothermal conditions. The authors studied in detail the ferrimagnetic ordering and other magnetic properties of this product, comparing them with those of both natural and synthetic greigite samples published before. Later on, Li *et al.* [3] described the surfactant-assisted hydrothermal procedure with cetyltrimethylammonium bromide (CTAB) as the surfactant and cysteine as the sulphur source, which provided pure greigite samples with a crystallite edge length of ≈ 1 μm. In order to prepare nanocrystalline greigite of high purity, Pashchenko *et al.* [6] adapted this procedure and varied the surfactants and their concentrations, obtaining samples with the mean size of crystallites of 30 and 80 nm.

The transport properties of greigite were investigated primarily on polycrystalline samples fabricated by cold isostatic pressing of hydrothermally prepared particles, e.g., the ≈ 1 μm sized grains prepared by Li *et al.* [3] or 0.5 μm thick platelets by P. Li *et al.* [7]. In addition, we may note a single report to our knowledge on the transport properties of thin film of greigite that was prepared by the vacuum deposition method. This material was used in the paper of Nozaki [8] for the study of electric conductivity and magnetoelectric phenomena like Hall effect. The results have shown that intrinsic conduction of Fe₃S₄ is a metallic one.

As concerns the potential applications, the ferrimagnetic order and relatively high saturation magnetization at room temperature of 67.2 emu/g [3], combined with the low toxicity of greigite, made Fe₃S₄ nanoparticles a promising material for medical therapy and diagnostics, such as cancer treatment

*Corresponding author: knizek@fzu.cz

245129-1

by magnetic hyperthermia, magnetic resonance imaging, and magnetically guided drug delivery [9,10]. Further, Cao *et al.* [11], Paolella *et al.* [12], and Li *et al.* [3] studied electrochemical properties of nanosized greigite by using cyclic voltammetry and galvanostatic discharge-charge cycling, and pointed out its potential use as an anode in lithium-ion batteries. The metallic nature of greigite and its strong magnetism up to elevated temperatures are attractive also in view of applications in electronics and spintronics [3,13–15]. However, one of the limiting factors to reveal all the potentials of greigite is the general lack of good-quality samples in bulk forms needed for fundamental research, especially for transport measurements.

In an attempt to provide data that could contribute to an understanding of the electric transport behaviors and the role of extrinsic factors in them and, simultaneously, considering the will to maximize the phase purity of resulting ceramics, nanogranular samples have been fabricated by cold isostatic pressing of nanocrystallites of two distinct sizes prepared according to Pashchenko *et al.* [6]. The present study involves measurements of diverse transport properties, in which the nanogranular greigite is characterized as a metallic conductor strongly influenced by local defects (mean free path at $T \to 0$ K is 0.2 nm only). We argue that the thermal conductivity inside the grains has a significant contribution from both phonon and magnon dynamics at cryogenic temperatures, and, in addition to standardly low diffusive thermopower, there is an observable contribution to Seebeck effect due to mutual magnon-electron drag. Special attention is given to the role of intergrain boundaries, through which electrons may penetrate by quantum tunneling, and heat is transmitted by the long-wavelength lattice and surface phonons.

In the next parts, the investigation is focused on Nernst (NE) and Hall (HE) effects. They both refer to transverse transport, i.e., the situation when two external fields, arranged along two perpendicular axes of the sample, induce entropy or charge density flows along the third axis of the sample. One of these fields is the thermal gradient for the Nernst effect, whereas it is the DC electric field for the Hall effect, and the other one is the magnetic field $\vec{B}$ or spontaneous magnetization $\vec{M}$. The transverse transport is generally revealed as the Nernst or Hall voltage due to accumulation of positive and negative charges on opposite sides of the sample in the direction of the third axis. The observed data distinguish between effects of the ordinary (ONE, OHE) and anomalous (ANE, AHE) kinds, and are interpreted by evoking Onsager reciprocal relations for the particle and heat flows in formulations of Callen and others [16–18].

II. ELECTRONIC STRUCTURE CALCULATIONS

Let us first discuss the thiospinel Fe_3S_4 in comparison with its oxide counterpart Fe_3O_4, known as the mineral magnetite. Both systems possess crystal structure of the space group symmetry $Fd\bar{3}m$. Compared to $a = 8.394$ Å for magnetite, the lattice parameter for greigite is significantly larger making $a = 9.872$ Å at room temperature [3]. Oxygen or sulfur atoms form a face-centered-cubic network, in which iron atoms occupy 1/8 of the tetrahedral interstices (*A* sites) and 1/2 of the octahedral interstices (*B* sites); see the structure
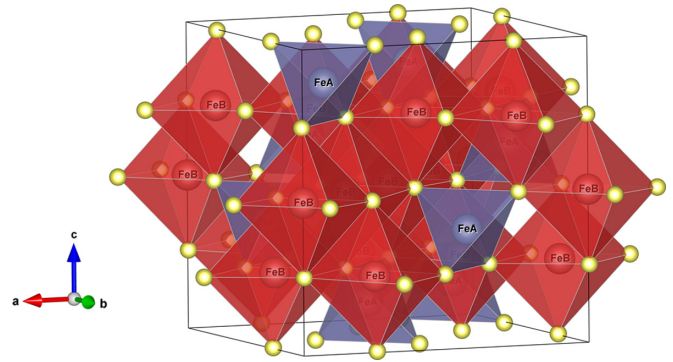

FIG. 1. Spinel structure of Fe_3S_4 and Fe_3O_4. Blue tetrahedra of Fe_A, red octahedra of Fe_B, and yellow spheres of *S* or *O* are shown. Space group $Fd\bar{3}m$, atom positions Fe_A: 1/8, 1/8, 1/8 (8*a*), Fe_B: 1/2, 1/2, 1/2 (16*d*), S/O: *x*, *x*, *x* (32*e*).

displayed in Fig. 1. In the ferrimagnetic configuration, the iron spin moments on *A* sites are oriented antiparallel to the spins on *B* sites. The moments observed of Fe_3O_4 at low temperature are very slightly lower compared to the theoretical values for Fe^{3+} in *A* sites ($m_A = 4.44\mu_B$), and for Fe^{2+}/Fe^{3+} mixture in *B* sites ($m_B = 4.17\mu_B$), which results in saturated ferrimagnetic moment $m = 2m_B - m_A$ of $3.9\mu_B$/f.u. (f.u. = formula unit Fe_3O_4) [19]. On the other hand, the ferrimagnetic moments reported for thiospinel Fe_3S_4 samples are lower, with the highest reported saturation magnetization of $3.74\mu_B$/f.u. at 5 K according to Li *et al.* [3]. More important data come from the neutron diffraction study [5], in which spontaneously ordered moments in both the *A* and *B* sublattices are determined, $m_A = 3.0\,\mu_B$ and $m_B = 3.25\,\mu_B$, with total moment calculated to $\sim 3.5\,\mu_B$/f.u. The ordering temperature T_C is rather uncertain because of the instability of greigite at high temperature and has been estimated to 600–670 K [15].

Large differences are also in the character of charge carriers. The experimental study of the greigite thin film by Nozaki [8] showed ordinary Hall resistivity practically independent on temperature in the range 4.3–297 K, $R_O = 3.4 \times 10^{-11}$ Ω cm/G (or 3.4×10^{-9} m³/C), pointing to the *p*-type carriers of concentration 0.22 hole per f.u. (hole concentration of 1.8×10^{21} cm⁻³). For magnetite measured at room temperature (in the regime of small polaron hopping), the Hall resistivity is found to be negative, $R_O = -2.12 \times 10^{-11}$ Ω cm/G (or -2.12×10^{-9} m³/C). This allows a lower estimate of the carrier concentration at RT to be 0.22 electron per f.u. ($\sim 3.0 \times 10^{21}$ cm⁻³) [20,21].

To get more insight, we performed detailed electronic structure calculations for Fe_3S_4 and Fe_3O_4. The calculations were made with the WIEN2K program [22] based on the density functional theory (DFT). It uses the full-potential linearized augmented plane-wave (FP LAPW) method with the dual basis set. In the LAPW method, the space is divided into nonoverlapping atomic spheres and the interstitial region. For the exchange correlation potential, we adopted the generalized gradient approximation (GGA) form [23], including an orbitally dependent potential for 3*d* orbitals implemented in the GGA+*U* method [24]. This method uses two additional parameters, namely Hubbard energy *U*
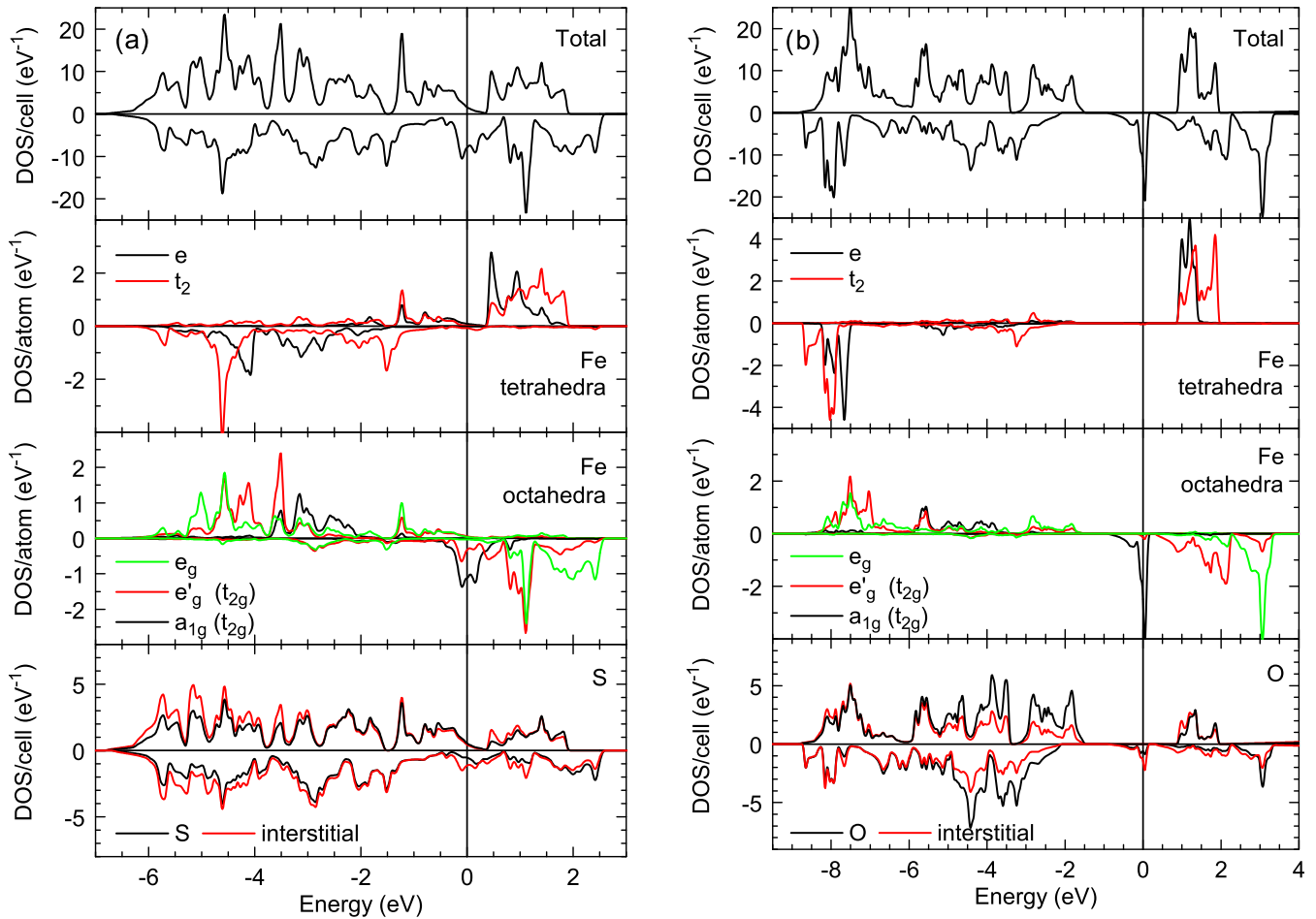
FIG. 2. The spin-majority (up) and spin-minority (down) total and projected DOS for (a) Fe_3S_4 and (b) Fe_3O_4.

describing Coulomb repulsion of electrons in the same orbital and Hund's exchange parameter J, which is approximately 1 eV independently on the system studied. Several values of U over the range 0–3 eV were tested for the sulphide. Increasing U resulted in increased magnetic moments on each Fe site as well as the increased total moment. The value of the Hubbard energy $U = 2$ eV was finally chosen; the criterion for this choice was the best agreement between the calculated and experimentally observed magnetic moment of the greigite [3]. The calculated densities of states (DOSs) for Fe_3S_4 are displayed in Fig. 2(a). A higher value of $U = 5.4$ eV was used for the DOS calculation for the partner oxide Fe_3O_4 and is related to the fact that the correlation effects are generally stronger in oxides than in sulphides [25]. The calculated DOSs for Fe_3O_4 are displayed in Fig. 2(b). Our values of U and J are similar to values $U_{eff} = U - J = 0.7$ and 3.6 used in [7], and $U_{eff} = 1.0$ and 3.8 used in [26,27] for Fe_3S_4 and Fe_3O_4, respectively, and $U = 2.5$ and $J = 1$ eV used in [28] for Fe_3S_4.

The atomic charges and magnetic moments were calculated using the atoms in molecule (AIM) concept of Bader [29]. In this approach, the unit cell is divided into regions by surfaces that run through the minima in the charge density. By integrating the electron or spin density within these regions the charge or spin moment on a given site can be calculated. The advantage of this method is that the analysis is based

solely on the charge or spin density so it is independent of the basis set and atomic spheres used.

The structural parameters were optimized during the self-consistent cycles. The resulting lattice parameters $a = 9.9173$ and 8.4030 Å are by 0.4% and 0.1% larger than experimental values, and the coordinates of the S/O site (x, x, x) are $x = 0.2548$ and 0.2544, for Fe_3S_4 and Fe_3O_4, respectively. For Fe_3O_4, one may notice an existence of a large gap in the spin-majority states, and a smaller moment and charge located on the B site compared to the A site; see Table I. These findings confirm the inverse spinel structure, $(Fe^{3+})_A[Fe^{2.5+}_2]_B O_4$. Let us note that the AIM method takes into account the charge transfer between cation and ligands, therefore the calculated charges are lower than the ideal ones,

TABLE I. Charges and magnetic moments calculated for individual atoms using the AIM method [29]. A site: tetrahedral; B site: octahedral.

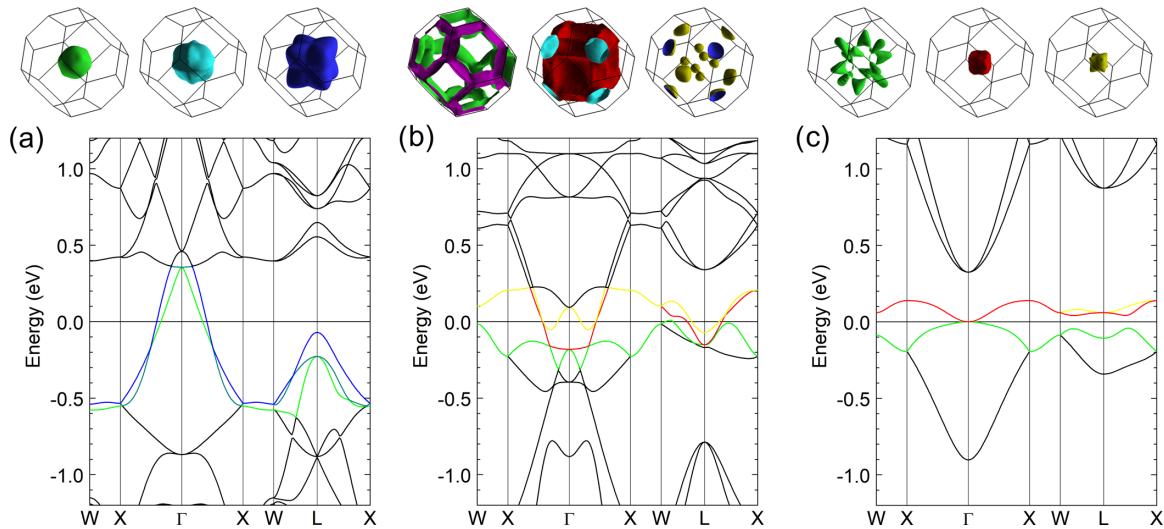|	Charges			Spin moments			
	Fe_A	Fe_B	S/O	Total	Fe(A)	Fe(B)	S/O
Fe_3S_4	1.00	1.07	−0.79	3.73	−3.54	3.61	0.01
Fe_3O_4	1.77	1.68	−1.28	4.00	−4.46	4.27	−0.02

FIG. 3. Multiband character of carriers and corresponding Fermi surfaces in (a) Fe_3S_4 majority spin, (b) Fe_3S_4 minority spin, (c) Fe_3O_4 minority spin. The bands forming the Fermi surfaces are highlighted by corresponding colors.

depending on the degree of covalency. The energy splitting of the antibonding d orbitals of the B site, which are located around and above the Fermi level, is governed by the crystal field of the trigonally elongated octahedral, i.e., t_{2g} orbitals split into a_{1g} and e'_g orbitals. Spin-minority carriers in the narrow band at the Fermi level are entirely of a_{1g}-orbital origin mixed with ligand orbitals. This is in agreement with the half-metallic conduction (or perhaps the magnetic-polaron hopping) attributed to magnetite above the Verwey temperature of ≈ 120 K. On the other hand, the gap in thiospinel Fe_3S_4 is suppressed and the Fermi level possesses both the spin-minority and spin-majority carriers, which means that Fe_3S_4 should be thus considered as a normal metal (see also [7]). The a_{1g}-orbital character of the spin minority carriers still prevails, whereas the spin majority carriers are mainly contributed by the tetrahedral A-site orbitals mixed with octahedral and sulphur orbitals. Another difference is manifested in the charges and magnetic moments, which are higher in the B site than in the A site, in agreement with the neutron diffraction study of Fe_3S_4 [5]. This signifies a stabilization of intermediate-type structure between the inverse and normal spinel, with iron charges distributed evenly among A and B sites.

The difference between the sulphide and oxide is readily seen in the electron band spectra and corresponding Fermi surfaces presented in Fig. 3. It appears that in contrast to three spin-minority Fermi surfaces of n-type carriers in half-metal Fe_3O_4, there are three spin-minority and three spin-majority Fermi surfaces in Fe_3S_4. In order to shed light onto such a complex situation with carriers of many bands contributing, the results of the electronic structure calculations for Fe_3S_4 have been further utilized as input data for computing electronic properties by means of the BOLTZTRAP program [30]. The parameters actually calculated are (a) linear coefficient of electronic heat capacity $\gamma_{calc} = 3.0$ mJ mol^{-1} K^{-2}, (b) average effective mass for carriers at spin-minority and spin-majority Fermi surfaces $m^* = 10m_e$ and $13m_e$, respectively, and (c) average Fermi velocities $v_F = 1.5 \times 10^5$ and 2.0×10^5 m/s, respectively. The carriers of both spins are dominantly of p

type and the spin-minority contribution to overall conductivity exceeds to about 20% the spin-majority contribution. In what follows, the computed transport properties are discussed with respect to experimental findings in Secs. IV A–IV C below.

III. PREPARATION AND CHARACTERIZATION OF THE NANOGRANULAR Fe_3S_4

As the experimental part of this study is concerned, the preparation of greigite nanocrystallites of controlled size was carried out according to our previous paper [6] with only minor modification (two to three higher concentrations of $FeCl_2$ and cysteine were employed in the present case to yield a sufficient amount of the product for transport measurements). The preparation procedure was based on the aforementioned surfactant-assisted hydrothermal method developed by Li *et al.* [9], but the surfactants and their amounts were varied to achieve greigite crystallites of a size on the nanoscopic scale. The use of cetyltrimethylammonium bromide (CTAB) at a concentration of 67 mmol/L (compared to 17 mmol/L in the study [9]) led to the mean crystallite size of $d_{XRD} \approx 80$ nm according to the x-ray diffraction line broadening, whereas the application of oleic acid at 106 mmol/L provided particles with $d_{XRD} \approx 30$ nm. Detailed characterizations of the two greigite products as concerns the morphology, chemical composition, and valence distribution were already reported [6], and thus only a short summary follows here. Importantly, both the powder samples were compacted by applying cold isostatic pressing, which provided samples suitable for transport measurements in the present study.

The x-ray diffraction data were acquired using a powder Bruker D8 Advance diffractometer with Cu-$K\alpha$ radiation equipped with a Lynxeye XE-T detector. The x-ray diffraction patterns of the present products showed characteristic lines for the greigite spinel structure with the $Fd\bar{3}m$ symmetry. The sample with 80 nm crystallites was assessed as single spinel phase material without any crystallized impurity phases characterized by lattice parameter $a = 9.8714(1)$ Å. In contrast to the previous report, the sample with 30 nm crystallites
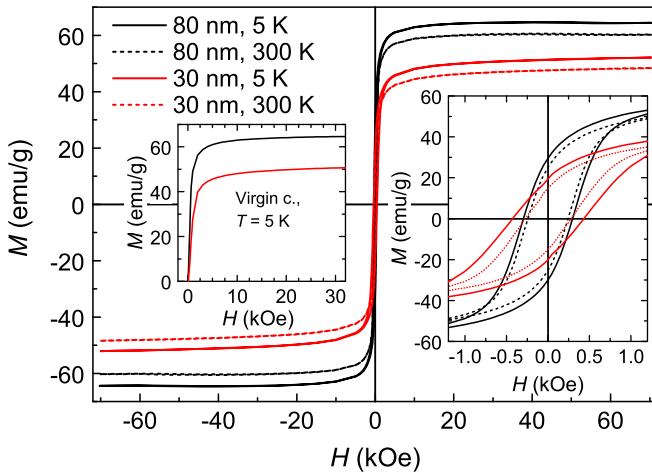
FIG. 4. Low and room temperature magnetization curves of Fe_3S_4 nanocrystallites compacted by cold isostatic pressing. The left inset shows the virgin curves at 5 K, the right inset displays low-field details of the hysteresis loops at 5 and 300 K.

contained about 8 wt % of marcasite FeS_2 as minor admixture. This fact likely resulted from nonoptimal conditions of the synthesis at higher concentration of starting materials, which was, however, necessary to obtain a sufficient amount of material for the transport measurements. Nevertheless, the 30 nm sample exhibited a practically identical $a = 9.8724(2)$ Å.

The magnetic response was measured using a superconducting quantum interference device (SQUID) magnetometer (MPMS, Quantum Design). Magnetic properties of the consolidated samples are illustrated in Figs. 4 and 5 (for more details on magnetism of the comparable samples, see [6]). The data in Fig. 4 evidence relatively large magnetization, making 64.6 and 51.5 emu/g at 5 K in magnetic field of 5 T for 80 and 30 nm crystallites, respectively. The value observed for the larger nanocrystallites is very close to the low-temperature
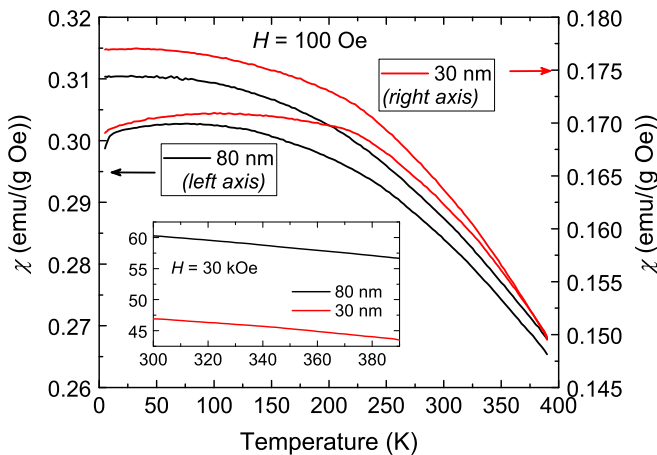

FIG. 5. Temperature dependencies of magnetic susceptibility of the compacted samples Fe_3S_4 in the range 5–390 K and magnetization between 300 and 390 K. The main graph shows the ZFC scan and susceptibility during subsequent cooling in magnetic field of 100 Oe, whereas the inset displays the magnetization in field of 30 kOe.

magnetizations of 63.3–70.6 emu/g (3.39–3.74 μ_B/f.u.) reported for the high purity greigite samples with larger grains [3,4]. The magnetization decreases with increasing temperature rather modestly, in particular to about 7% at 300 K and 13% at the highest experimental temperature of 390 K. The smaller low-temperature magnetization of the sample with 30 nm crystallites, decreased also compared to the value 59.7 emu/g reported by Pashchenko et al. [6] for the sample of the same crystallite size, is partially an effect of nonferromagnetic surface layer that commonly affects the magnetization in nanosize, and partially it can be attributed to a small amount of the antiferromagnetic marcasite impurity. The susceptibility data in Fig. 5 reveal some differences between the two samples related to the distinct size of their crystallites. Based on the field-cooled (FC) and zero-field-cooled (ZFC) curves, we infer a practically blocked state of the larger crystallites in the whole temperature range under study, whereas the sample with smaller crystallites enters the superparamagnetic state at the highest temperatures with the irreversibility point (the bifurcation of the ZFC and FC curves) of ≈ 370 K.

The transport properties measurements were performed on nanogranular samples of greigite prepared by cold isostatic pressing of nanoparticles of larger or smaller mean crystallite size ($d_{XRD} \approx$ 80 or 30 nm). The pressed samples were cut to the required size using a diamond saw. The electrical contacts were made with a nickel paste, which is more suitable in the case of sulphur-containing materials than a silver paste forming nonconductive sulfides.

The measurements of longitudinal transport properties, i.e., electrical resistivity, thermal conductivity, and thermopower (Seebeck coefficient $V_x/\Delta T_x$), were performed using the four-probe method thermal transport option (TTO) of the physical property measurement system (PPMS, Quantum Design) on a specimen of length $L_x = 8$ mm and 2×2 mm^2 cross section.

As regards the measurements of transverse transport properties, the measurement of Hall effect was also performed on PPMS apparatus (for the sample of 80 nm crystallite size only), whereas the Nernst effect on both samples was measured using a home-made apparatus. The small voltage signal V_y was measured using a Keithley 2182A nanovoltmeter and the temperature difference ΔT_x was detected by differential thermocouples at the hot and cold sides of the samples. The geometry was employed in which the magnetic field $\vec{B}$ is applied parallel to the z axis, the electric current (I-Hall effect) or the temperature increment (ΔT-Nernst effect) are applied along the x axis, and the induced voltage is measured in the y direction; see also the insets of Fig. 10. For measurement of Hall resistivity V_y/I_x, the thickness of the greigite sample was $L_z = 0.5$ mm and the dimensions in the direction of electric current and detected voltage were $L_x = L_y = 4$ mm. The measurement of Nernst coefficient $V_y/\Delta T_x$ was done on a sample with $L_z = 2$ mm, the dimension in the direction of applied temperature gradient $L_x = 2$ mm, and the electric contact distance to detect transverse voltage $L_y = 4$ mm. The Nernst signal S_{yx} was calculated according to a formula

$$S_{yx} = \frac{E_y}{\nabla T_x} = \frac{V_y}{L_y} \frac{L_x}{\Delta T_x} \quad (\mu V/K).$$
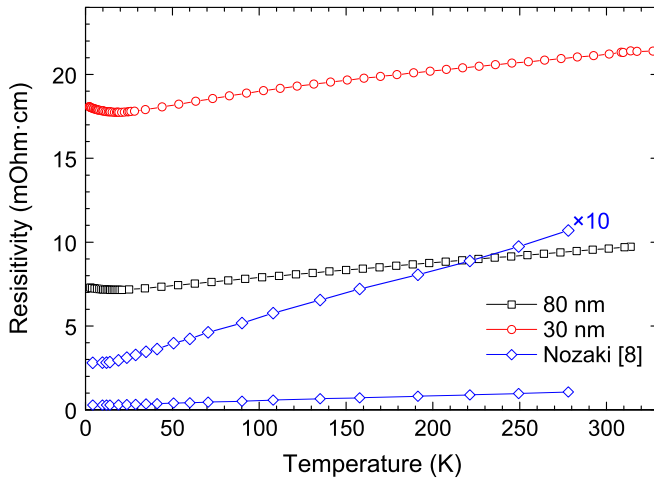
FIG. 6. The temperature dependence of electrical resistivity of the compacted samples Fe_3S_4 compared with data from Ref. [8].

The results of all transport measurements are presented and discussed in detail in Secs. IV A–IV E.

IV. TRANSPORT PHENOMENA

A. Electrical resistivity

Temperature dependence of resistivity measured on the isostatically pressed samples of 80 and 30 nm crystallite sizes is plotted in Fig. 6. For samples with larger crystallite size, the resistivity character is metallic over the whole range 4–390 K, and the absolute value of 9.7 mΩ cm at room temperature is significantly smaller than values reported for analogous nanogranular materials earlier, but still exceeds by one order of magnitude the resistivity obtained by Nozaki on vacuum deposited film [8]. For sake of comparison, the latter data are reproduced in Fig. 6 as the best example of greigite resistivity up to date.

One may note that the temperature dependence for greigite film (blue diamond in Fig. 6) is typical for a true metal. Employing a simple approach, we analyze the temperature dependence of resistivity as a sum of two terms. The first one is the temperature independent part that reflects scattering on defects in the film and is manifested as residual resistivity for $T \rightarrow 0$ K making 0.28 mΩ cm. Comparing this value with the electronic structure determination combined with BOLZTRAP calculations, we have arrived at a relaxation time for defect scattering in greigite film of $\tau = 7$ fs. With the velocity of charge carriers at Fermi level determined to be $v_F \approx 200$ km/s, this relaxation time corresponds to a mean free path of 1.4 nm. The second resistivity term is the standard part due to electron-phonon scattering, the temperature dependence of which revokes the Bloch-Grueneisen formula (see, e.g., [31]) and is characterized with T^n dependence at very low temperatures (actually $n = 4.1$) gradually changing to the linear T dependence at elevated temperatures with a slope of 2.9×10^{-3} mΩ cm/K. The resistivity reaches 1.07 mΩ cm at 278 K. A useful comparison with noble metals can be made—e.g., the annealed 99.999% pure gold shows a residual resistivity of $\rho_o = 0.02$ $\mu\Omega$ cm, the increase at low temperatures obeys the Bloch-Grueneisen formula with ideal

exponent $n = 5$,[1] and the room-temperature resistivity makes $\rho_{RT} = 2$ $\mu\Omega$ cm [31]. Similarly for pure iron as the most common example of an itinerant ferromagnet, $\rho_o = 0.248$ $\mu\Omega$ cm, $\rho_{RT} = 10$ $\mu\Omega$ cm, and $n = 3$ [32]. In these two metals, the resistivity drops more or less to two orders of magnitude between 300 and 4 K, while for greigite film there is only a fourfold difference. This is indicative for the more important role of electron scattering by defects/impurities in the greigite film.

In contrast to the vacuum deposited greigite film, the present nanogranular sample of 80 nm crystallites shows resistivity of linear dependence in nearly the whole temperature range with a slope of 8.8×10^{-3} mΩ cm/K, and the $T \rightarrow 0$ extrapolated residual resistivity makes the large value of 7.3 mΩ cm. (The respective values for the 30 nm size sample are 12×10^{-3} mΩ cm/K and 18 mΩ cm.) These findings open a question of whether increased resistivity with respect to the greigite film is due to some enhanced scattering within the nanograins, or it can be attributed to intergrain barriers through which the charge carriers penetrate by quantum tunneling. Most importantly, if the transmission probability of tunneling were the only reason for the resistivity increase, both the residual part ρ_o and slope would be changed to same factor. In fact, they are increased in the sample of 80 nm grains by a factor of 26 and 3, respectively. This is an argument for our conjecture that the presence of barriers increases the bulk conductivity by a factor 3, and the dominating factor 26/3∼9 refers to the enhanced defect scattering inside grains. We thus conclude that the resistance of the grain barrier is twice larger than the resistance of the grain itself,[2] and the internal resistivity of 80 nm grains at $T \rightarrow 0$ makes 2.4 mΩ cm, corresponding to an electron mean free path of 0.2 nm only. A similar electron free path can be anticipated also for the 30 nm sample, since its ∼2.5 larger residual resistivity nicely equals the size ratio, and can be thus fully attributed to an increased number of intergrain crossings. With the electron mean free path being close to the interatomic distance in the Fe_3S_4 structure, both nanogranular samples can be considered as threshold metallic conductors in the sense of the Ioffe-Regel criterion.

At the lowest temperature limit, an upturn of the resistivity is seen in Fig. 6 for nanogranular greigite samples, which presumably indicates the localization of carriers due to the presence of an intergranular Coulomb gap; see the

---

[1]The Bloch-Grüneisen formula is derived for monovalent metal with a spherical Fermi surface and phonon spectrum derived from a Debye model: $\rho_{e-p} = \frac{C}{M\theta} (\frac{T}{\theta})^5 \int_0^{\theta/T} \frac{x^5 e^x}{(e^x - 1)^2} dx$, where θ is the Debye temperature, M is the atomic weight, and C is a constant of the metal.

[2]With grain barriers making 2/3 of bulk resistivity and the number of intergrain crossings in the 80 nm greigite sample ($\sim 1.25 \times 10^5$ cm^{-1}), the resistivity per unit area of single barrier is calculated to be 3.8×10^{-9} Ω cm^2. Some comparison can be made with widely studied polycrystalline and nanogranular samples of La-Sr manganites, also of the ferromagnetic metallic state. Here, the resistivity of the barrier has been found to be more than three orders of magnitude larger [37], which can be related to the poorly conducting shell (thickness of about 1 nm) that is present intrinsically at the manganite surface. The greigite grains are evidently conducting homogeneously up to the top layer.
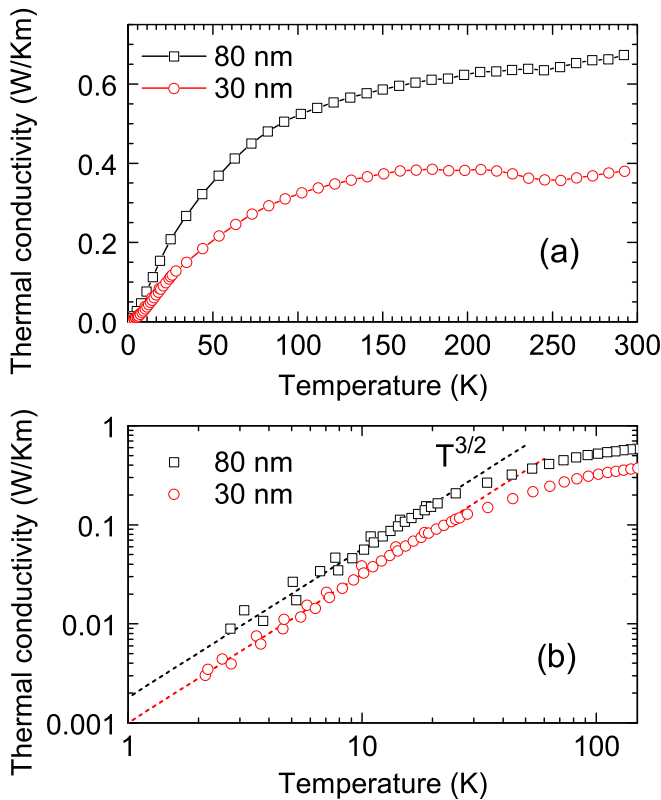
FIG. 7. (a) The temperature dependence of thermal conductivity of the compacted samples Fe_3S_4. (b) The same data in the log-log plot.

FIG. 8. The low-temperature heat capacity measured on the Fe_3S_4 sample of 80 nm crystallite size.

theoretically predicted localization $\ln\rho \approx T^{-1/2}$ by Helman and Abeles [33] and its experimental manifestation collected, e.g., for polycrystalline manganites of small grain sizes [34,35]. Such weak localization possibly obscures eventual manifestations of electron-magnon scattering, characterized at low enough temperatures by resistivity of the T^2 or T^3 dependence, for conventional itinerant ferromagnets and half-metals, respectively [36]. The T^5 resistivity term predicted at low temperatures for electron-phonon scattering by Bloch-Grueneisen formula is unlikely because phonon dynamics is suppressed by defects/imperfections highly pronounced at low temperatures.

B. Thermal conductivity

The temperature dependence of thermal conductivity is shown in Fig. 7. There is a steep initial rise at the lowest temperatures but starting from 20 to 30 K, the rate of the increase is gradually diminished until a flat maximum at 100–250 K is reached. As expected, the absolute values actually observed are smaller for samples with smaller grains and finally, above ∼250 K, the thermal conduction slightly increases again, possibly due to extrinsic effects (parasitic radiation of the sample and/or radiation thermal transport between grains). The behavior close to the lowest temperature limit is more readily demonstrated in the log-log plot in Fig. 7(b) where the thermal conductivity for both nanogranular greigite samples follows a T^n dependence with $n = 1.5$ in a remarkably broad temperature range up to ∼20 K. As a complementary experiment, we
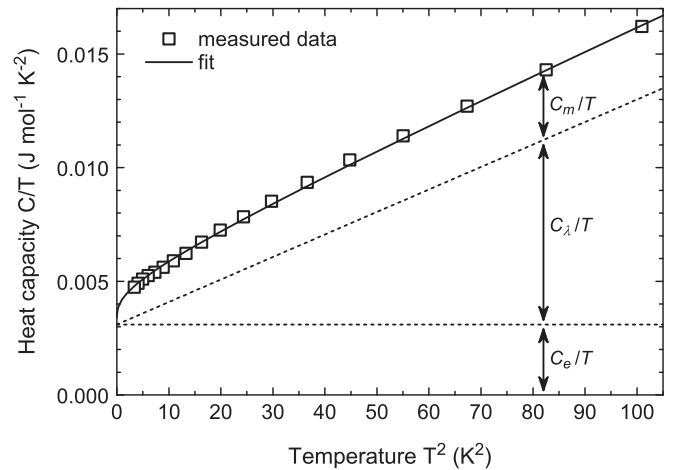
present in Fig. 8 the measurement of low-temperature specific heat of the 80 nm sample.

The interpretation of thermal conductivity in greigite is complicated since thermal properties of itinerant ferromagnets, in general, are essentially influenced by strong coupling of the spin and electronic excitations, further by correlated character of carriers, size dependent effects, etc. A simplified model, applicable at low temperatures, then anticipates three additive contributions: the electronic term κ_e due to flow of quasifree charge carriers induced by applied temperature gradient, and two bosonic terms κ_λ and κ_m corresponding to heat transport by lattice phonons and magnons, respectively, leading in total to

$$\kappa = \kappa_e + \kappa_\lambda + \kappa_m.$$

Analogous three terms are considered also for heat capacity,

$$C_{\text{tot}} = C_e + C_\lambda + C_m,$$

that are known in theory as the heat capacity of electrons obeying Fermi statistics, the low-T lattice heat by phonons in the Debye model, and the low-T heat capacity of magnons with simple quadratic dispersion $\hbar\omega = Dq^2$ applicable for cubic greigite with ferrimagnetic order. Mathematically we have

$$C_e = \gamma T, \quad C_\lambda = 234 r N_A k_B \left(\frac{T}{\Theta_D}\right)^3, \quad \text{and}$$

$$C_m(T) = 0.113 V_{\text{mol}} k_B \left(\frac{k_B T}{D}\right)^{3/2},$$

where $r = 7$ is the number of atoms in formula unit and $V_{\text{mol}} = N_A a^3/8 = 72.4 \times 10^{-6} \text{ m}^3$ is the molar volume of Fe_3S_4.[3] The low temperature heat capacity data are shown

---

[3] The formula for magnon heat capacity, see, e.g., [38–40], is valid at zero magnetic field. With external field increasing, the magnons are gradually depopulated because of an energy gap of $g\mu_B B$ and the magnon heat is correspondingly diminished or might be completely

in Fig. 8. They are modeled (full line) as a sum of three terms, $C_{tot}(T) = \gamma T + \beta T^3 + \delta T^{3/2}$. The linear coefficient of electronic heat is determined to $\gamma = 3.1$ mJ mol^{-1} K^{-2}, in excellent agreement with the value calculated (see Sec. II), and fitted values β and δ lead to reasonable values of Debye temperature $\theta_D = 530$ K and spin-wave stiffness $D = 200$ meV Å^2, in agreement with previously published data.[4] As to the lattice and magnon heat capacity, the values $C_\lambda = 99$ mJ mol^{-1} K^{-1}(1365 J m^{-3} K^{-1}) and $C_m = 32$ mJ mol^{-1} K^{-1}(440 J m^{-3} K^{-1}) have been determined at 10 K.

Turning now to the thermal conductivity in greigite, we note that its electronic term is closely related to electric conductivity by the Wiedemann-Franz law $L_o = \kappa_e/\sigma T$ as exemplified, e.g., by measurements of thermal conduction in pure polycrystalline iron [32]. Ideal theoretical value of Lorentz number $L_o = 2.45 \times 10^{-8}$ V^2 K^{-2} was found to apply at least up to 20 K, where iron showed constant resistivity of $\rho_o = 0.248$ $\mu\Omega$ cm. In effect, the observed κ_e was T linear and made about 100 W m^{-1} K^{-1} at 10 K; see similar findings in the recent paper of Watzmann *et al.* [45]. The internal resistivity of the present 80 nm greigite grains in our estimation is 10^4 times larger ($\rho_o = 2.4$ mΩ cm), which means also that the electronic term of thermal conductivity in the grains is correspondingly lower, making $\kappa_e = 0.01$ W m^{-1} K^{-1} at 10 K. As bulk thermal conductivity of the nanogranular sample is concerned, the electronic contribution is further reduced by a factor 3 becoming negligible compared to the measured value at 10 K, $\kappa = 0.06$ W m^{-1} K^{-1}. This leads to the fact that, in contrast to pure iron where thermal conduction is almost completely electronic, the phonons and/or magnons have a dominant contribution in the nanogranular greigite samples. As concerns these bosonic terms, we refer to conventional kinetic gas theory reasonably applicable at low temperatures [38]. Within this approximation the thermal conductivity of the diffusive system, neglecting the role of grain boundaries, can be written as

$$\kappa = \kappa_e + \tfrac{1}{3}C_\lambda v_\lambda l_\lambda + \tfrac{1}{3}C_m v_m l_m,$$

where in the second term C_λ is the lattice specific heat per unit volume, v_λ is the group velocity of acoustic phonons (sound velocity), and l_λ is their mean free path, at low temperatures limited in ceramic nanocrystalline samples by their crystallite size. The third term is given by the magnon specific heat C_m, energy averaged magnon velocity of v_m, and the magnon free path l_m determined primarily by the crystallite size, taking into

account that magnons (as excitations of an exchange coupled system of local spins) do not suffer from defect scattering. As a rough estimate of v_m at least for determination of its T dependence, it is possible to consider the group velocity for thermal magnons ($\hbar\omega = k_B T$),

$$v_m(T) = \frac{d\omega}{dk} = 2\sqrt{\frac{D\omega}{\hbar}} = \frac{2}{\hbar}\sqrt{Dk_B T},$$

which gives altogether the theoretical T^2 dependence of thermal conductivity. The energy averaged group velocity v_m to use in kinetic gas formula is, nonetheless, 1.62 times larger,[5] which means that not the thermal but the superthermal magnons have the dominant contribution to κ_m.

Employing parameters obtained in the heat capacity measurement, v_λ estimated to 2000 m/s and v_m of dominant acoustic magnons calculated from $D = 200$ meV Å^2 to 6300 m/s at 10 K, we can thus determine the components of thermal conductivity inside the 80 nm grains of the greigite sample. The values calculated for 10 K are $\kappa_\lambda = 0.073$ W m^{-1} K^{-1} and $\kappa_m = 0.074$ W m^{-1} K^{-1} for the phononic and magnonic terms, respectively, which together with $\kappa_e = 0.010$ W m^{-1} K^{-1} allows us to estimate the total thermal conductivity inside grains to 0.16 W m^{-1} K^{-1}. Since bulk thermal conductivity measured at 10 K makes only about one-third of this, $\kappa = 0.06$ W m^{-1} K^{-1}, we quantify that in the 80 nm greigite sample the thermal resistivity of the grain boundary is twice larger than the thermal resistivity of the grain itself. Although our analysis is only a rough estimate at a particular temperature ($T = 10$ K), we may presume that transmission probabilities for electron (see our analysis of electrical resistivity in Sec. IV A) and heat flows through grain boundary are similar, or at least not dramatically different. This is a rather remarkable finding since the mechanisms of the boundary penetration are completely different—quantum tunneling of electrons vs transmission of heat through grain boundary by participation of some kind of nonequilibrium phonons.

A final remark concerns the dependence of thermal conductivity in the temperature range up to about 20 K. For the boundary limited transport with dominant contribution of phonons and magnons, the above outlined theory predicts a sum of T^3 and T^2 terms, but in reality a slower $T^{3/2}$ dependence is observed. Let us note that this seeming discrepancy is likely again an effect of grain boundaries as shown for purely phononic conductivity in silicon by decreasing its crystallite size [46,47], or for magnonic conductivity in the ferromagnetic insulator YIG [48,49]. It appears that only the long-wavelength lattice phonons and surface phonons can carry the heat through intergrain barriers, so that the bulk heat

---

quenched if temperature is sufficiently low; see for more details [41–43].

[4]The spin-wave stiffness $D = 200$ meV Å^2 corresponds to an alternatively used parameter $D' = D/a^2 = 2.05$ meV or 24 K in units of temperature ($a = 9.872$ Å). Let us note that there is no direct determination of magnon spectra in greigite. Nonetheless, Chang *et al.* [4] did estimate the mean spin wave stiffness from the temperature decrease of spontaneous magnetization, taking into account that $\delta M_s \sim T^{3/2}$ based on Bloch spin wave expansion; see also [44] for theoretical justification in the case of exchange interactions in ferrimagnetic spinels. A very similar value of $D = 193$ meV Å^2 was obtained.

---

[5]More rigorous treatment is based on proper integration over the q space, which gives the theoretical formula for magnonic conductivity in the case of the boundary limited free path l_m [39], $\kappa_m(T) = \frac{\zeta(3)k_B^3 l_m T^2}{\pi^2 \hbar D}$, where ζ is the Riemann zeta function ($\zeta(3) = 1.202$). Based on this, one may deduce that not the velocity of thermal magnons ($v_m = 3900$ m/s at 10 K) but 1.62 times larger velocity ($v_m = 6300$ m/s at 10 K) is the appropriate value for using the simplified kinetic gas formula.

transport cannot be simply derived from bosons in thermal equilibrium as assumed by the theory. This is also the reason why thermal conductivity tends quickly to a saturation above 100 K.

C. Thermoelectric power

The thermoelectric properties are commonly expressed through the Seebeck coefficient. In theory, the Seebeck coefficient is defined as the ratio of entropy flow to charge flow in the isothermal region but experimentally, an open circuit is used and one measures the voltage per temperature gradient at zero electric current. As shown below in Sec. IV E and the Appendix, the equivalence of both approaches follows from Onsager reciprocal relations valid for the electric and heat (entropy) currents in the presence of electromotive force and temperature gradient. Full treatment is given in the seminal paper of Callen [16] and presented recently in the book of Zlatić and Monnier [18].

As the itinerant ferromagnets are concerned, in addition to the generally very low diffusive thermopower given by the Mott expression $S_d = \frac{(\pi k_B)^2 T}{3e\sigma}(\frac{\partial \sigma}{\partial E})_{E_F}$, there is a contribution S_{md} from magnon dynamics. The latter contribution results from electron-magnon collisions that exert mutual drag between the electronic and magnonic systems, and such a magnon drag effect is known to boost thermopower in ferromagnetic metals such as Fe, Co, or Ni [45,46]. According to early theories, see, e.g., the paper of Bailyn [50], the magnon drag effect in thermopower is to a certain extent analogous to the effect of phonon drag whose treatment can be dated back to works of Klemens, Ziman, and Herring [51–53]. The simplest model presumes that electron-phonon or electron-magnon collisions set the drift velocity of phonons/magnons to be the same as the drift velocity of electrons. This principle, justified if there are no other dissipation processes, was developed further for the magnon drag and its suppression by high external field in the paper of Grannemann and Berger [42]. As to the occurrence of the drag phenomena, it should be noted that phonon drag is observed only in systems with minimum defects, whereas the presence of dopants or structural disorder (porosity, nanostructuring) suppresses both the low-temperature phononic peak in thermal conductivity and the drag effect in thermopower as demonstrated early in dilute copper alloys or by the difference between the annealed and unannealed nickel [54,55]. On the other hand, magnon drag is found to be robust and much more resistant to alloying and other defects as exemplified for ferromagnetic metals Fe, Co, and Ni of different microstructures [45,55]. Most importantly the magnon drag contribution S_{md} to thermopower starts at higher temperature than that common for phonon drag; in our case it develops a maximum at about 200 K ($\sim T_C/2$).

More recently, a hydrodynamic model of magnon drag was formulated by Watzman *et al.* [45] and applied for ferromagnetic metals. In this phenomenological model,[6] the electron and magnon systems are treated as two penetrating classical

FIG. 9. The temperature dependence of thermopower of the compacted samples Fe_3S_4.

gases (fluids), characterized by their number density, mass, and drift velocity. We remind that applying the conservation law of linear momentum during electron-magnon collisions (magnon umklapp scattering is neglected) provides the formula for S_{md}, that depends on the magnonic heat capacity C_m and electron-magnon scattering rate τ_{em}^{-1} confronted with scattering rate τ_m^{-1} due to dissipative magnon-to-lattice processes:

$$S_{md} = \frac{2}{3}\frac{C_m}{n_e e}\frac{\tau_{em}^{-1}}{\tau_{em}^{-1} + \tau_m^{-1}}.$$

Indeed, the Seebeck coefficient measured on the present nanogranular samples of greigite shown in Fig. 9 exhibits, in contrast to anticipated theoretical linear dependence for quasifree carriers, more complex temperature dependence. For samples with smaller grains, the Seebeck coefficient steeply rises from the lowest temperatures, then the slope is gradually diminished and a plateau of 4 μV/K is finally reached at 130 K and higher. On the other hand, the sample with larger grains shows a very small negative Seebeck coefficient at very low temperature (<0.5 μV/K). From about 30 K the Seebeck coefficient starts to rise to positive values and reaches above 100 K at a plateau of 2 μV/K. Let us note that the room temperature Seebeck coefficient reported for the greigite film by Nozaki, 3.6 μV/K, is not far from our data. As the overall temperature trend of Seebeck is concerned, there is some similarity to what is seen in the thermal conductivity in Fig. 7, which can be considered as a general argument for presence of magnon drag. In the present nanogranular samples

---

[6]Microscopic theory of magnon-drag thermopower was presented by Tserkovnyak and Mecklenburg [56], based on the spinmotive forces that are exerted on spins of conduction electrons when moving
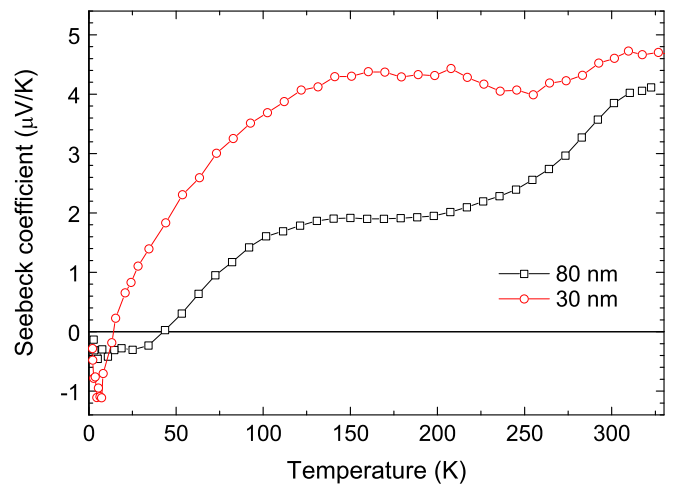
---

through a dynamic magnetization texture formed by orbital electrons of the itinerant ferromagnet (see also [57] and references therein). It is considered that long-wavelength magnons propagating from hot to cold represent analogous smoothly variable texture that interacts with conduction electrons via exchange interaction of finite strength, for which the itinerant spins cannot follow the dynamic magnetization vector ideally. The result is thus a kind of viscous drag that, importantly, exhibits driving force on conduction electrons in parallel or opposite direction to magnon flow, depending on their spin polarization.

there is also a question of the role of grain boundaries, but because of the fortuitous similarity of the electron and heat intergrain transmittivity mentioned above, the thermoelectric property measured on bulk should reflect the internal property of grains.[7]

In an attempt to interpret the thermopower data, we consider first that in nanogranular greigite, the electron-magnon collisions largely dominate over other scattering mechanisms of magnons ($\tau_{em}^{-1} \gg \tau_m^{-1}$). In this case, the magnon drag contribution to the Seebeck coefficient is given by a simpler formula that unifies the results derived based on different principles in Refs. [42,45]:

$$S_{md} = \frac{2}{3} \frac{C_m}{n_e e}.$$

With magnonic heat capacity C_m proportional to $T^{3/2}$, the magnon-drag contribution will increase with temperature similarly. Indeed, the Seebeck data measured on pure iron follow the $T^{3/2}$ trend over an exceptionally broad temperature range; see Watzmann *et al.* [45] for more details. However, no $T^{3/2}$ scaling can be drawn from the low-temperature Seebeck data on present greigite samples, and the role of magnon drag can be judged only indirectly from the similarity of the 100–250 K flat maximum in Figs. 7 and 9. Nonetheless, some illustrative estimate can be done based on the above-mentioned formula. With $C_m = 440 \, \mathrm{J\,m^{-3}\,K^{-1}}$ and $R_0 = 1/n_e e = 3.4 \times 10^{-9} \, \mathrm{m^3/C}$, the magnon drag thermopower of $S_{md} = 0.99 \, \mu\mathrm{V/K}$ is calculated for gregite at $T = 10 \, \mathrm{K}$, whereas the values measured on both the 80 and 30 nm samples at 10 K are significantly smaller and negative. This suggests that a realistic description of the magnon-drag effect should take into account more complex mechanisms in which linear momentum of magnons streaming from hot to cold is either absorbed directly by the grain boundary scattering or dissipated into a phonon bath in processes parametrized by Gilbert damping. This may lead, especially at low temperature, to $\tau_{em}^{-1} < \tau_m^{-1}$ and significant suppression of the magnon-drag contribution to thermopower [45].

D. Hall and Nernst experiments

In common metals, both the Hall resistivity and the Nernst coefficient derive from the Lorentz force imposed on propagating charge carriers proportionally to the strength of perpendicularly applied magnetic field, $\vec{F} = q\vec{v} \times \vec{B}$. Apart from this classical effect, the ferromagnetic systems exhibit extraordinary effects that arise due to mechanisms of quantum origins and are often more important. The experiments show that the magnitude of such anomalous contributions is proportional to the bulk magnetization and closely follows its hysteresis loops $M(H)$, which makes the separation of the normal and anomalous terms possible.

---

[7]There is also a question on the applicability of Onsager reciprocal relations for nanogranular systems in the situation when heat associated with electric current contains a contribution from phonon or magnon drag. In our opinion, the similar electron and heat transmittivity of grain boundaries in the material under study might assure an affirmative answer.
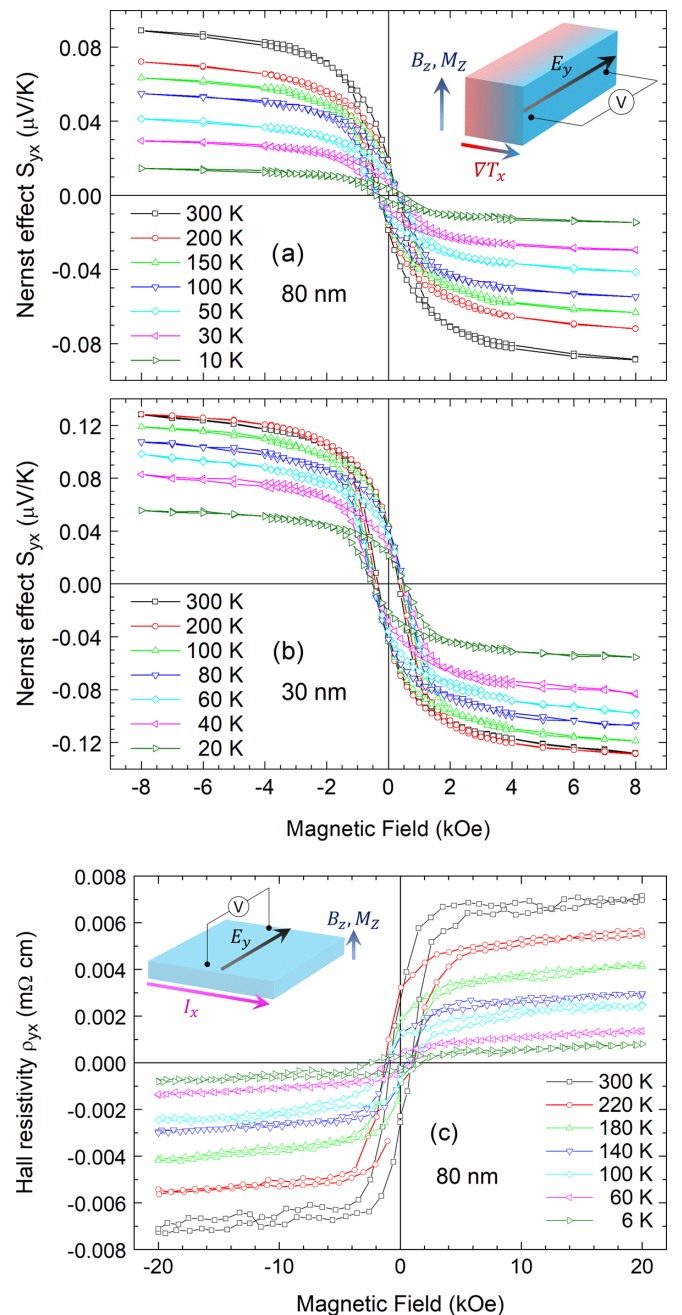

FIG. 10. Hysteresis curves of (a) Nernst effect of 80 nm sample. (b) Nernst effect of 30 nm sample. (c) Hall effect of 80 nm sample Fe_3S_4. The insets show the geometry of the experiments: temperature gradient ΔT_x, electric current I_x, resulting electric field E_y, magnetic field B_z, and magnetization M_z.

The data of Nernst coefficient $S_{yx} = V_y/\Delta T_x$, measured on the Fe_3S_4 samples of 80 and 30 nm particle size, and the data of Hall resistivity $\rho_{yx} = V_y/I_x$ on a sample of 80 nm particle size are presented in Fig. 10. One may distinguish the normal *H*-linear contribution (ONE, OHE) from the anomalous *M*-dependent (ANE, AHE) contribution that exhibits certain coercivity and saturates in low fields. The temperature dependencies of ONE and ANE are shown in Fig. 11, and OHE and AHE compared with data of Nozaki [8] are shown in Fig. 12. It is worthwhile to note that the ordinary and anomalous
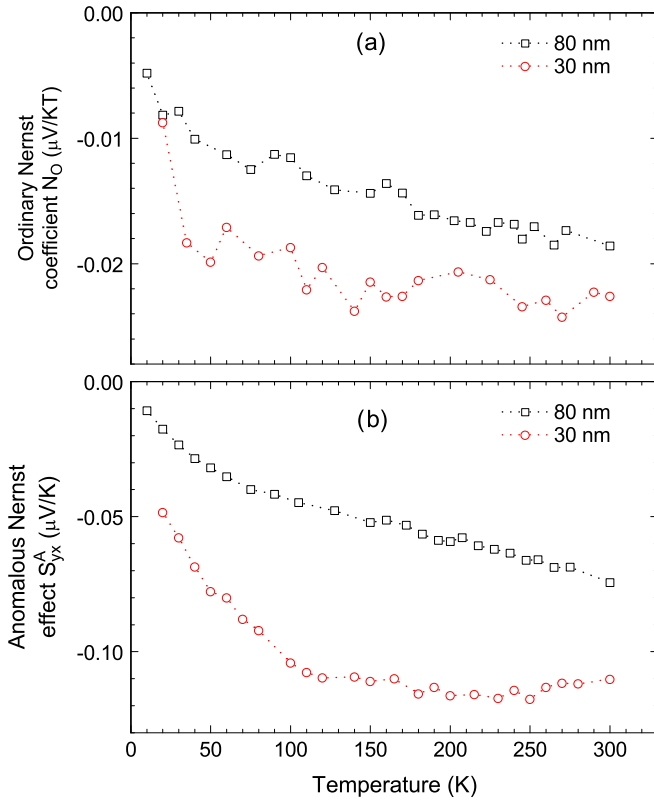
FIG. 11. The temperature dependence of (a) the ordinary Nernst coefficient $N_O = S_{yx}^O/B$, and (b) anomalous Nernst effect S_{yx}^A of the compacted samples Fe$_3$S$_4$.
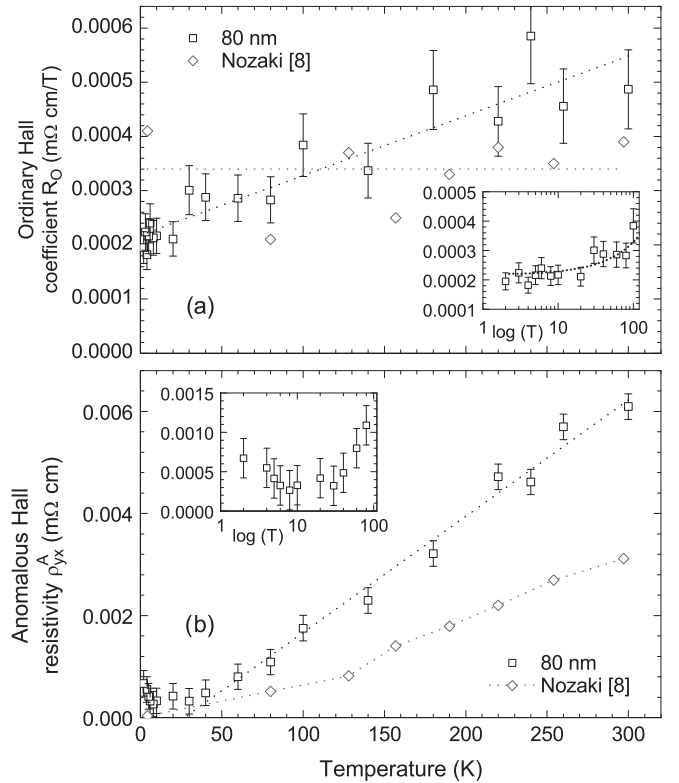

FIG. 12. The temperature dependence of (a) the ordinary Hall coefficient $R_O = \rho_{yx}^O/B$, compared with data from Ref. [8], (b) the anomalous Hall resistivity ρ_{yx}^A compared with data from Ref. [8]. The insets show a detailed view of the low temperature data in $\log(T)$ scale.

Nernst effects in Fe$_3$S$_4$ are negative, whereas the Seebeck coefficient and both Hall effects are positive. This is exactly opposite to Fe$_3$O$_4$ that displays negative Seebeck and Hall effects, and positive Nernst effects [58].

The absolute value of anomalous Nernst effect of the 30 nm sample is approximately twice bigger than that of the 80 nm sample; see Fig. 11. Interestingly, a similar difference of their Seebeck coefficients is observed; see Fig. 9. This suggests that thermogalvanic phenomena in metallic greigite have in addition to a standard diffusive part also another contribution (the magnon drag) that is evidently size dependent. The temperature dependence of the ANE of the 80 nm sample is almost linear, whereas that of the 30 nm sample is practically constant down 100 K and then also decreases almost linearly. Both tend towards zero at the lowest temperature. The behavior of the ordinary Nernst effect is similar, i.e., the 30 nm sample exhibits a higher absolute value than the 80 nm sample and both decrease towards zero with lowering temperature.

As the ordinary Hall resistivity is concerned, one may see a clear decrease with decreasing temperature; see Fig. 12. Consequently, a direct simple translation of R_H to carrier concentration based on a single parabolic band approximation is thus delicate; moreover, theoretical calculations point to a coexistence of several Fermi surfaces and their complex shapes (see Fig. 3). Nozaki, however, claimed the observation of a temperature independent Hall resistivity with, most importantly, very comparable mean value that translates to $\sim$0.2 holes/f.u.; see Fig. 12(a), blue diamonds. In the lower

panel of Fig. 12 the displayed anomalous Hall resistivity also slopes down with decreasing temperature to a minimum between 30 and 10 K and it rises slightly again at the lowest temperatures. Thus, the temperature dependence of the anomalous Hall resistivity closely resembles that of longitudinal resistivity, which also displays a minimum around 15 K after its quasilinear decrease from room temperature.

E. Interpretation of Hall and Nernst effects within the linear transport theory

In an attempt to interpret the transverse transport in greigite we refer first to the original Callen treatment of thermomagnetic and galvanomagnetic phenomena [16]. This is based on generalized Onsager equations for planar flows of charge and heat (J_x^e, J_y^e, J_x^Q, J_y^Q) in the presence of perpendicular magnetic field. In these phenomenological equations, four forces expressed through the gradients of electrochemical potentials ($\frac{1}{T}\nabla_x\mu$, $\frac{1}{T}\nabla_y\mu$) and temperature ($\nabla_x\frac{1}{T}$, $\nabla_y\frac{1}{T}$) are the proper variables to assure the validity of famous reciprocal relations between kinetic coefficients for the flows. It appears that for a system with physical isotropy in the x,y plane there are just six independent kinetic coefficients. Considering the metallic nature of greigite and using slightly different notation (see, e.g., the recent book of Zlatić and Monnier [18]), the equations can be presented through components

of electric field and temperature gradients as given in the Appendix.[8]

Based on the Onsager equations, various transport phenomena and the interrelation between them can be evaluated for different experimental setups (isothermal/adiabatic conditions, open/closed circuits). In the present work, the Hall resistivity $\rho_{yx} = V_y/I_x$ is measured under isothermal conditions ($\nabla_x T = \nabla_y T = 0$), which is assured by sticking the greigite sample to a copper block with thin insulating spacer. The Nernst coefficient is most readily also defined at isothermal conditions as transverse entropy density current induced by longitudinal charge density current, $S_{yx} = (J_y^Q/J_x^e)/T$, analogously to the standard definition of Seebeck coefficient as entropy current per electric current, $S_{xx} = (J_x^Q/J_x^e)/T$. In practice, Seebeck and Nernst are nonetheless measured with open circuit by detecting voltage that is induced by applied temperature gradient. The theory shows that there is an equivalency $(J_x^Q/J_x^e)/T = (V_x/\Delta T_x)_i$ and $(J_y^Q/J_x^e)/T = (V_y/\Delta T_x)_i$, where the index i means "isothermal" in the y direction ($\Delta T_y = 0$). The real setup is, however, much closer to the "adiabatic" case ($J_y^Q = 0$). In such a case, the actual effect is given by $(V_y/\Delta T_x)_a = (V_y/\Delta T_x)_i - S_{xx}R$, where $R = \nabla_y T/\nabla_x T$ is a measure of Righi-Leduc effect in the absence of electric current (see, e.g., [17]); the difference is nonetheless negligible in most metals.

As shown in detail in the Appendix, the longitudinal and transverse phenomena can be expressed, neglecting higher order terms, through six basic parameters. These are the electrical resistivity (or conductivity) $\rho_{xx} \sim 1/\sigma_{xx}$ and $\rho_{yx} \sim \sigma_{xy}/\sigma_{xx}^2$, thermal conductivity κ_{xx} and κ_{xy}, and so-called thermoelectric conductivity α_{xx} and α_{yx} [see Eq. (A5)], all having a direct relation to kinetic coefficients for charge and heat flows.

It should be noted that thermal conductivity κ_{xx} as given in Eq. (A3a) and actually measured refers to an open electrical circuit, i.e., the thermal flow is hindered by the presence of Seebeck voltage, $V_x/\Delta T_x = \rho_{xx}\alpha_{xx}$. The electronic term of thermal conductivity is thus diminished by the amount of $-\rho_{xx}\alpha_{xx}^2 = -\sigma_{xx}S_{xx}^2$. Neglecting such a correction may negatively influence the reliability of the Lorentz number studies on well-conducting systems with a large Seebeck coefficient. The situation with nanogranular greigite is, however, very different. The overall thermal conductivity of the 80 nm sample at 300 K makes about $\kappa_{xx} = 0.6\,\mathrm{W\,K^{-1}\,m^{-1}}$. It is dominated by the magnonic term while other contributions are largely suppressed by defect scattering in nanogranular Fe_3S_4. This concerns the lattice or acoustic-phonon thermal conductivity and the electronic term that is related to the room-temperature conductivity $\sigma_{xx} = 1.0 \times 10^4\,\mathrm{S/cm}$ by Wiedemann-Franz law ($k_e = 0.13\,\mathrm{W\,K^{-1}\,m^{-1}}$ at 300 K) and is theoretically diminished, due to Seebeck voltage, by an amount of $-\rho_{xx}\alpha_{xx}^2 = -\sigma_{xx}S_{xx}^2$ ($S_{xx} = 3.0\,\mu\mathrm{V/K}$). The effect calculated for greigite, $\Delta k_e = -1.0 \times 10^{-8}\,\mathrm{W\,K^{-1}\,m^{-1}}$ at 300 K, is really negligible, and this holds to a still larger extent at low temperatures.
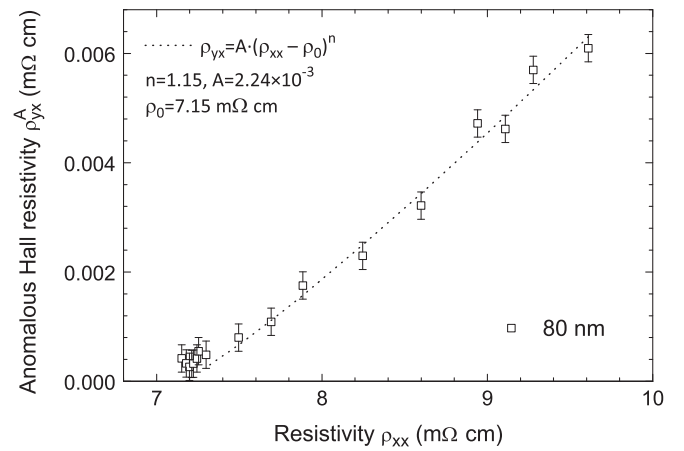

FIG. 13. The dependence of the anomalous Hall resistivity vs longitudinal resistivity.

A counterpart of common electrical resistivity ρ_{xx} is the transverse phenomenon of Hall resistivity $\rho_{yx} = V_y/I_x$. Its value varies linearly with applied field H_z or in the case of AHE, with bulk magnetization M_z. Several models linking anomalous Hall resistivity ρ_{yx}^{AH} and longitudinal resistivity ρ_{xx} have been devised in the form $\rho_{yx}^{AH} \sim \lambda \rho_{xx}^n$, with n and λ as nondimensional exponent and prefactor [59]. The intrinsic models that only depend on the ideal band structure and are independent of scattering include interband effect and Berry phase mechanisms. The models based on extrinsic mechanisms include side jump and skew scattering. The models can be distinguished by the exponent n in the above mentioned power-law relation. The intrinsic and side jump mechanisms can be modeled with the exponent $n = 2$. In contrast, the skew-scattering mechanism predicts $n = 1$. The experiment on the 80 nm sample of Fe_3S_4 allows us to make a check of the scaling character of ρ_{xx} and the AHE part of ρ_{yx} based on their temperature dependent data. As shown in Fig. 13, there is nearly linear dependence between the longitudinal and transverse conductivities. Our fit by a power law $\rho_{yx}^A(T) = A\,[\rho_{xx}(T) - \rho_{xx}(0)]^n$, where $\rho_{xx}(0)$ is the rather high residual resistivity due to grain boundary and static defect scattering, gives $n = 1.15$, which is close to $n = 1$ predicted by the skew-scattering mechanism.

The Nernst coefficient linearly dependent on H_z or M_z has been the main focus of the present study. In general, it is defined as $(V_y/\Delta T_x)_i = \rho_{yx}\alpha_{xx} + \rho_{xx}\alpha_{yx}$; see the tensor formula for Seebeck and Nernst, $S = \sigma^{-1}\alpha$, in the Appendix [Eq. (A5)]. Nonetheless, the values measured in the standard way require correction for the above-mentioned Righi-Leduc term $S_{xx}\frac{\nabla_y T}{\nabla_x T} \sim \rho_{xx}\alpha_{xx}\kappa_{xy}/\kappa_{xx}$ that is always present but difficult to determine. To our knowledge, the only direct measurement of Righi-Leduc effect in an itinerant ferromagnet was achieved for iron metal and its alloys [60–62], using the fact that their thermal conductivity is almost exclusively of the electronic type. It was shown that (a) in analogy to the Wiedemann-Franz law relating the thermal and electronic conductivities, there is a similar relation between the transverse conductivity κ_{xy} and Hall conductivity σ_{xy}, quantified by Lorentz number not far from the ideal L_0 value; (b) for both κ_{xy} and σ_{xy} the ordinary (H_z-dependent) and anomalous
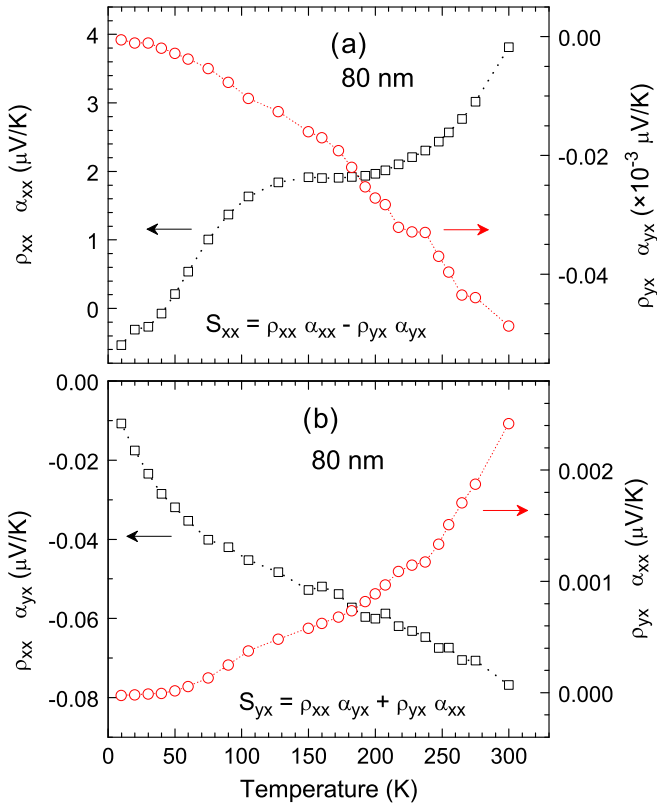

FIG. 14. Components of (a) Seebeck coefficient $S_{xx} = \rho_{xx}\alpha_{xx} - \rho_{yx}\alpha_{yx}$ and (b) anomalous Nernst effect $S_{yx} = \rho_{xx}\alpha_{yx} + \rho_{yx}\alpha_{xx}$.

FIG. 15. (a) The dependence of the anomalous transverse electrical conductivity vs longitudinal electrical conductivity corrected by ρ_0 (see Fig. 13). (b) The dependence of the anomalous transverse thermoelectric conductivity vs longitudinal thermoelectric conductivity.

(M_z-dependent) components can be distinguished—the latter ones having dominant contribution at least for experimental fields below 100 kOe; (c) the magnitude of κ_{xy} at $B = 3\,\mathrm{T}$, i.e., well above the magnetic saturation of iron, is significantly lower than longitudinal thermal conductivity κ_{xx}, with a ratio (Righi-Leduc coefficient) varying from about $1/100$ at 300 K to about $1/1000$ at 5 K.

For greigite we can anticipate still lower values of $\nabla_y T/\nabla_x T = \kappa_{xy}/\kappa_{xx}$ than found in the iron metal, presumably because the electronic part in κ_{xx} is overwhelmed with much larger magnonic contribution. The correction for Righi-Leduc effect, involving also Seebeck coefficient of rather low value of $\sim 3\,\mu$V/K for greigite at 300 K, becomes thus negligible. It is thus seen that irrespective of the "isothermal" or "adiabatic" regime, the Nernst coefficient can be analyzed as a sum of two parts that are presented in the Appendix and have been widely used in the literature, $\rho_{xx}\alpha_{yx} + \rho_{yx}\alpha_{xx}$.[9] Based on the present ANE data in combination with AHE, it is possible to separate these two parts. Their temperature dependence is seen in the lower panel of Fig. 14. It is seen that the term $\rho_{xx}\alpha_{yx}$, dependent on the transverse component of thermoelec-

tric conductivity, has a dominant contribution of negative sign and its absolute value increases steeply from zero value and acquires an almost linear trend above ~ 100 K. On the other hand, the minor term $\rho_{yx}\alpha_{xx}$ has positive sign and its originally very slow trend is accelerated with increasing temperature. It is worthwhile to note that analogous two parts can be considered also for the Seebeck coefficient, $S_{xx} = \rho_{xx}\alpha_{xx} - \rho_{yx}\alpha_{yx}$, where the second term arises as the reciprocal response of Onsager equations in the x-y plane.[10] It is quadratic dependent on M_z and its relative impact on the Seebeck value for greigite is negligible, $\sim 10^{-5}$ according to the data presented in Fig. 14(a).

In order to get more insight into the relation between the longitudinal and transverse parameters in the electric conductivity and thermoelectric conductivity, let us finally turn to the tensor form of Onsager kinetic equations for electric current

---

[9]As seen in the Appendix, the formula $S_{yx} = \rho_{xx}\alpha_{yx} + \rho_{yx}\alpha_{xx}$ follows from Onsager kinetic equations. Its use is justified at least in the case of ONE, where the transverse parameters ρ_{yx} and α_{yx} are both proportional to H_z by virtue of the Lorentz force. When applied for ANE, rather formally, analogous transverse parameters dependent on M_z are anticipated.
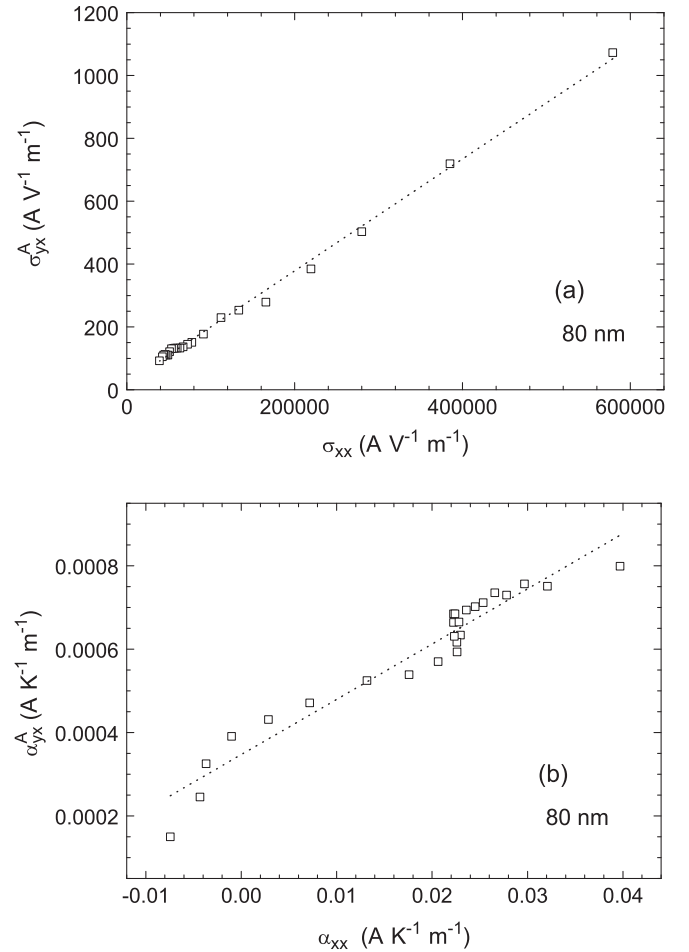
[10]In this respect we refer to an equivalent but intuitively more obvious form of Seebeck coefficient, $S_{xx} = \rho_{xx}\alpha_{xx} + \rho_{xy}\alpha_{yx}$; see the thermoelectric tensor in the Appendix [Eq. (A5)].

given in the Appendix,

$$\vec{j}_e = \sigma \vec{E} + \alpha(-\vec{\nabla}T).$$

The components of primary interest for us and actually available for the 80 nm greigite sample are the adjusted values $\sigma_{xx}(T) = \frac{1}{\rho_{xx}(T) - \rho_{xx}(0)}$, calculated values $\alpha_{xx}(T)$, and values of anomalous Hall and Nernst components, $\sigma_{xy}^A(T) = \frac{\rho_{yx}^A}{\rho_{xx}^2}$ and $\alpha_{yx}^A(T)$. The data plotted in Fig. 15 show a similar quasilinear increasing trend for both the electric and thermoelectric conductivities, which can be understood as an independent proof of unique mechanism of anomalous, M_z-dependent effects in nanogranular greigite—the skew scattering.

V. CONCLUSIONS

Electronic structure calculations for iron sulphide Fe_3S_4 (greigite) have shown that compared to the oxide counterpart Fe_3O_4 (magnetite) of half-metallic character with n-type carriers at three spin-minority Fermi surfaces, there is a broader conduction band due to much larger hybridization between the iron $3d$ states and ligand s states and complex contribution of p-type carriers at three spin-minority and three spin-majority Fermi surfaces. Experimental investigations of the ferromagnetic ordering and transport properties (including the electric and thermal conductivity, the Hall, Seebeck, and Nernst effects) have been performed on two nanogranular greigite samples prepared by cold isostatic pressing of Fe_3S_4 particles with the mean crystallite size of $d_{XRD} \approx 80$ and 30 nm. The bulk conduction of nanogranular greigite is metalliclike with large residual value $\rho_0 = 7.3$ mΩ cm and nearly linear increase to higher temperatures with a slope of 8.8×10^{-3} mΩ cm/K for the 80 nm sample. Combining with resistivity data measured in earlier study on a unique thin-film sample of Fe_3S_4 we have estimated that in our nanostructured samples the electrical resistivity is formed from 1/3 by intragrain resistance and from 2/3 by intergrain barriers. Importantly, a similar ratio was obtained for the thermal resistance, when the experimental thermal conductivity was compared with calculated conductivity of grains themselves. This is a rather unique finding since background mechanisms are quite different—the quantum tunneling of electrons through barriers vs heat transfer due to transmittivity of long-wavelength phonons and contribution of surface phonons. The Seebeck coefficient measured on the 80 nm sample is rather low, but clear signs of magnon drag contributions have been found, leading to a broad maximum of $S \sim 2.0$ μV/K in temperature range $T = 100$–250 K.

The main attention has been given to transverse transport phenomena, which included the measurements of Hall and Nernst effects in magnetic fields from -1 to 1 T, the determination of their ordinary and anomalous parts, and the interpretation of the data in terms of fundamental kinetic coefficients of Onsager equations. The observed ordinary part of Hall resistivity for the 80 nm sample is weakly temperature dependent, corresponding to p-type conduction and on average $\sim$0.2 hole/f.u. in Fe_3S_4, which is in contrast to the n-type carriers in Fe_3O_4. The anomalous Hall shows complex behavior up to $\sim$20 K, which is followed with rather steep, almost T-linear increase at higher temperatures. The ordinary

and anomalous Nernst coefficients increase from their zero value for $T \rightarrow 0$ K in a nearly linear manner. It is of interest that Fe_3S_4 displays positive Seebeck and Hall effects and negative Nernst effects, whereas Fe_3O_4 displays exactly opposite signs of these effects.

The anomalous Nernst data for Fe_3S_4 have been separated into two distinct terms predicted by theory, the dominant one dependent on the transverse component and the minor one dependent on the longitudinal component of thermoelectric conductivity. The temperature dependent values of the former term provide an alternative way to check scaling of the thermoelectric conductivity components, analogously to widely used scaling between the longitudinal and transverse components of the electrical resistivity. It is concluded that the anomalous Hall and Nernst effects in nanogranular greigite are governed by skew scattering.

APPENDIX

Kinetic equations for the charge current density and heat current density in the presence of perpendicular magnetic field can be expressed, when applied to metals, in the following form [see, e.g., Eq. (5.2) in the book of Zlatić and Monnier [18]]:

$$J_x^e = +L_{11}^{xx}E_x + L_{11}^{xy}E_y - L_{12}^{xx}\frac{\nabla_x T}{T} - L_{12}^{xy}\frac{\nabla_y T}{T},$$

$$J_y^e = -L_{11}^{xy}E_x + L_{11}^{xx}E_y + L_{12}^{xy}\frac{\nabla_x T}{T} - L_{12}^{xx}\frac{\nabla_y T}{T},$$

$$J_x^Q = +L_{12}^{xx}E_x + L_{12}^{xy}E_y - L_{22}^{xx}\frac{\nabla_x T}{T} - L_{22}^{xy}\frac{\nabla_y T}{T},$$

$$J_y^Q = -L_{12}^{xy}E_x + L_{12}^{xx}E_y + L_{22}^{xy}\frac{\nabla_x T}{T} - L_{22}^{xx}\frac{\nabla_y T}{T}.$$

The present equations take already into account the Onsager reciprocal relations and are applicable for systems with physical isotropy in the x,y plane. The role of chemical potential is considered as negligible and the gradient of electric potential is included as $E_x = -\frac{1}{T}\nabla_x\Phi$ and $E_y = -\frac{1}{T}\nabla_y\Phi$. There are just six independent kinetic coefficients: L_{11}^{xx}, L_{12}^{xx}, and L_{22}^{xx} are even functions of the magnetic field, while the coefficients L_{11}^{xy}, L_{12}^{xy}, and L_{22}^{xy} are odd functions of the magnetic field or in the case of zero-field ANE or AHE, even and odd functions of the bulk magnetization M_z. (It is supposed that these latter coefficients are linearly dependent on H_z and M_z.) For our purposes, these four equations can be suitably

rewritten into the next form (see also [17]),

$$E_x = \rho_{xx} J_x^e + \rho_{xy} J_y^e + S_{xx} \nabla_x T + S_{xy} \nabla_y T, \quad \text{(A1a)}$$

$$E_y = \rho_{yx} J_x^e + \rho_{yy} J_y^e + S_{yx} \nabla_x T + S_{yy} \nabla_y T, \quad \text{(A1b)}$$

$$J_x^Q = T S_{xx} J_x^e + T S_{xy} J_y^e - \kappa_{xx} \nabla_x T - \kappa_{xy} \nabla_y T, \quad \text{(A1c)}$$

$$J_y^Q = T S_{yx} J_x^e + T S_{yy} J_y^e - \kappa_{yx} \nabla_x T - \kappa_{yy} \nabla_y T, \quad \text{(A1d)}$$

which include new parameters that are expressed through original kinetic coefficients and can be further simplified by neglecting terms depending on H_z (M_z) to higher order than linear,

$$S_{xx} = S_{yy} = \frac{1}{T} \frac{L_{11}^{xx} L_{12}^{xx} + L_{11}^{xy} L_{12}^{xy}}{\left(L_{11}^{xx}\right)^2 + \left(L_{11}^{xy}\right)^2} \sim \frac{1}{T} \frac{L_{12}^{xx}}{L_{11}^{xx}}, \quad \text{(A2a)}$$

$$S_{yx} = -S_{xy} = \frac{1}{T} \frac{L_{11}^{xy} L_{12}^{xx} - L_{11}^{xx} L_{12}^{xy}}{\left(L_{11}^{xx}\right)^2 + \left(L_{11}^{xy}\right)^2} \sim \frac{1}{T} \frac{L_{11}^{xy} L_{12}^{xx} - L_{11}^{xx} L_{12}^{xy}}{\left(L_{11}^{xx}\right)^2}, \quad \text{(A2b)}$$

$$\kappa_{xx} = \kappa_{yy} = \frac{L_{22}^{xx}}{T} - L_{12}^{xx} S_{xx} + L_{12}^{xy} S_{xy} + \kappa_\lambda + \kappa_m$$

$$\sim \frac{L_{22}^{xx}}{T} - L_{12}^{xx} S_{xx} + \kappa_\lambda + \kappa_m, \quad \text{(A3a)}$$

$$\kappa_{xy} = -\kappa_{yx} = \frac{L_{22}^{xy}}{T} - L_{12}^{xy} S_{xx} + L_{12}^{xx} S_{yx}, \quad \text{(A3b)}$$

$$\rho_{xx} = \rho_{yy} = \frac{L_{11}^{xx}}{\left(L_{11}^{xx}\right)^2 + \left(L_{11}^{xy}\right)^2} \sim \frac{1}{L_{11}^{xx}}, \quad \text{(A4a)}$$

$$\rho_{yx} = -\rho_{xy} = \frac{L_{11}^{xy}}{\left(L_{11}^{xx}\right)^2 + \left(L_{11}^{xy}\right)^2} \sim \frac{L_{11}^{xy}}{\left(L_{11}^{xx}\right)^2}. \quad \text{(A4b)}$$

All these parameters have a straightforward relation to transport properties. According to Eqs. (A1a) and (A1b), the parameter ρ_{xx} refers to common electrical resistivity and $\rho_{yx} = E_y / J_x^e$ is the Hall resistivity, both measured under isothermal conditions. As seen in Eqs. (A1c) and (A1d), S_{yx} is the Nernst coefficient defined at isothermal conditions as transverse entropy current induced by longitudinal electric current, $S_{yx} = (J_y^Q / J_x^e)/T$, analogously to the standard definition of Seebeck coefficient as entropy current per electric current, $S_{xx} = (J_x^Q / J_x^e)/T$. In a more practical way, Seebeck and Nernst are commonly measured with open circuit as voltage induced by applied temperature increment, considering the equality $(J_x^Q / J_x^e)/T = (E_x / \nabla_x T)_i$ and $(J_y^Q / J_x^e)/T = (E_y / \nabla_x T)_i$, where the index i means "isothermal" in the y direction ($\nabla_y T = 0$)—see Eqs. (A1a) and (A1b).

Finally, there are the longitudinal and transverse thermal conductivities κ_{xx} and κ_{yx} that quantify the heat current J_x^Q in response to temperature gradients $\nabla_x T$ and $\nabla_y T$. The longitudinal component as actually given in Eq. (A3a) is the total thermal conductivity measured with open electrical circuit. It is generally a sum of three terms—the electronic κ_e, phononic κ_λ, and magnonic κ_m. The theoretical value of the electronic term, $\kappa_e = L_{22}^{xx}/T$, is related to conductivity σ through the Lorentz number, $L_o = \kappa_e / \sigma T$ ($L_o = 2.45 \times 10^{-8}$ V^2 K^{-2}). When measured, it is partially reduced by the onset of Seebeck voltage; see the additional H-linear term $-L_{12}^{xx} S_{xx}$ in

Eq. (A3a). The reduction is, nonetheless, small for metallic systems. The transverse component κ_{yx} refers to two effects that are closely interrelated—the Righi-Leduc and so-called thermal Hall effects. The first one is quantified as transverse $\nabla_y T$ induced by longitudinal $\nabla_x T$, and is measured with open electrical circuit ($J_x^e = 0$) and the absence of transverse currents ($J_y^e = J_y^Q = 0$). The formula for the Righi-Leduc effect can be then written in two alternative ways:

$$\frac{\nabla_y T}{\nabla_x T} = \frac{\kappa_{xy}}{\kappa_{xx}} = \frac{\mathrm{w}_{xx}}{\mathrm{w}_{yx}},$$

where the first formulation derives from Eq. (A1d) and uses the components of thermal conductivity, whereas the second one is given in terms of thermal resistivity,

$$w_{xx} = w_{yy} = \kappa_{xx}/\left(\kappa_{xx}^2 + \kappa_{xy}^2\right) \sim 1/\kappa_{xx} \quad \text{and}$$

$$w_{yx} = -w_{xy} = \frac{\kappa_{xy}}{\left(\kappa_{xx}^2 + \kappa_{xy}^2\right)} \sim \frac{\kappa_{xy}}{\kappa_{xx}^2}.$$

The transverse component w_{yx} can be named as thermal Hall resistivity. Namely, it is intimately related to the thermal Hall effect, $w_{yx} = -\nabla_y T / J_x^Q$, which is an analog of standard Hall effect with electric current replaced by thermal current J_x^Q and electromotive force replaced by thermal force $-\nabla_y T$.

We may conclude that transport phenomena in the isotropic x, y plane, measured in the presence of perpendicularly acting magnetic field or spontaneous magnetization, can be suitably expressed through three tensors, containing in total six independent elements. These are the tensors of electrical resistivity ρ (or electric conductivity σ), thermoelectric conductivity α, and thermal resistivity w (or thermal conductivity κ). For galvanomagnetic properties one gets

$$\begin{pmatrix} E_x \\ E_y \end{pmatrix} = \begin{pmatrix} \rho_{xx} & \rho_{xy} \\ \rho_{yx} & \rho_{yy} \end{pmatrix} \begin{pmatrix} J_x^e \\ J_y^e \end{pmatrix} \quad \text{or equivalent,}$$

$$\begin{pmatrix} J_x^e \\ J_y^e \end{pmatrix} = \begin{pmatrix} \sigma_{xx} & \sigma_{xy} \\ \sigma_{yx} & \sigma_{yy} \end{pmatrix} \begin{pmatrix} E_x \\ E_y \end{pmatrix},$$

where $\sigma_{xx} = \sigma_{yy} = \rho_{xx}/(\rho_{xx}^2 + \rho_{yx}^2) \sim 1/\rho_{xx}$ and $\sigma_{xy} = -\sigma_{yx} = \rho_{yx}/(\rho_{xx}^2 + \rho_{yx}^2) \sim \rho_{yx}/\rho_{xx}^2$. For thermomagnetic properties like Seebeck and Nernst (given as $S = \sigma^{-1}\alpha$ in tensor notation),

$$\begin{pmatrix} E_x \\ E_y \end{pmatrix} = \begin{pmatrix} \rho_{xx}\alpha_{xx} + \rho_{xy}\alpha_{yx} & \rho_{xx}\alpha_{xy} + \rho_{xy}\alpha_{yy} \\ \rho_{yx}\alpha_{xx} + \rho_{yy}\alpha_{yx} & \rho_{yx}\alpha_{xy} + \rho_{yy}\alpha_{yy} \end{pmatrix} \begin{pmatrix} \nabla_x T \\ \nabla_y T \end{pmatrix}, \quad \text{(A5)}$$

where $\alpha_{xx} = \alpha_{yy} = \frac{L_{12}^{xx}}{T}$ and $\alpha_{xy} = -\alpha_{yx} = \frac{L_{12}^{xy}}{T}$. Finally for the thermal Hall,

$$\begin{pmatrix} -\nabla_x T \\ -\nabla_y T \end{pmatrix} = \begin{pmatrix} w_{xx} & w_{xy} \\ w_{yx} & w_{yy} \end{pmatrix} \begin{pmatrix} J_x^Q \\ J_y^Q \end{pmatrix}.$$

[1] M. Farina, D. M. S. Esquivel, and H. Debarros, Magnetic iron-sulfur crystals from a magnetotactic microorganism, Nature (London) **343**, 256 (1990).

[2] S. Mann, N. H. C. Sparks, R. B. Frankel, D. A. Bazylinski, and H. W. Jannasch, Biomineralization of ferrimagnetic greigite (Fe_3S_4) and iron pyrite (FeS_2) in a magnetotactic bacterium, Nature (London) **343**, 258 (1990).

[3] G. Li, B. Zhang, F. Yu, A. A. Novakova, M. S. Krivenkov, T. Y. Kiseleva, L. Chang, J. Rao, A. O. Polyakov, G. R. Blake, R. A. de Groot, and T. T. M. Palstra, High-Purity Fe_3S_4 greigite microcrystals for magnetic and electrochemical performance, Chem. Mater. **26**, 5821 (2014).

[4] L. Chang, A. P. Roberts, Y. Tang, B. D. Rainford, A. R. Muxworthy, and Q. Chen, Fundamental magnetic parameters from pure synthetic greigite (Fe_3S_4), J. Geophys. Res. **113**, B06104 (2008).

[5] L. Chang, B. D. Rainford, J. R. Stewart, C. Ritter, A. P. Roberts, Y. Tang, and Q. Chen, Magnetic structure of greigite (Fe_3S_4) probed by neutron powder diffraction and polarized neutron diffraction, J. Geophys. Res. **114**, B07101 (2009).

[6] M. Pashchenko, P. Veverka, T. Kmječ, O. Kaman, L. Kubíčková, J. Kohout, M. Klementová, O. Kravchuk, A. Vakula, S. Tarapov, J. Hejtmánek, and K. Knížek, Magnetic, FMR and Mössbauer studies of nanocristalline greigite, J. Alloy. Compd. **857**, 157569 (2021).

[7] P. Li, C. Xia, Q. Zhang, Z. B. Guo, W. Y. Cui, H. L. Bai, H. N. Alshareef, and X. X. Zhang, Fabrication and characterization of nanostructured Fe_3S_4, an isostructural compound of half-metallic Fe_3O_4, J. Appl. Phys. **117**, 223903 (2015).

[8] H. Nozaki, Galvanomagnetic properties of Fe_3S_4, J. Appl. Phys. **51**, 486 (1980).

[9] M. Feng, Y. Lu, Y. Yang, M. Zhang, Y. J. Xu, H. L. Gao, L. Dong, W. P. Xu, and S. H. Yu, Bioinspired greigite magnetic nanocrystals: Chemical synthesis and biomedicine applications, Sci. Rep. **3**, 2994 (2013).

[10] J. Liu, X. Guo, Z. Zhao, B. Li, J. Qin, Z. Peng, G. He, D. J. L. Brett, R. Wang, and X. Lu, Fe_3S_4 nanoparticles for arterial inflammation therapy: Integration of magnetic hyperthermia and photothermal treatment, Appl. Mater. Today **18**, 100457 (2020).

[11] F. Cao, W. Hu, L. Zhou, W. Shi, S. Song, Y. Lei, S. Wang, and H. Zhang, 3D Fe_3S_4 flower-like microspheres: High-yield synthesis via a biomolecule-assisted solution approach, their electrical, magnetic and electrochemical hydrogen storage properties, Dalton Trans. **42**, 9246 (2009).

[12] A. Paolella, C. George, M. Povia, Y. Zhang, R. Krahne, M. Gich, A. Genovese, A. Falqui, M. Longobardi, P. Guardia, T. Pellegrino, and L. Manna, Charge transport and electrochemical properties of colloidal greigite (Fe_3S_4) nanoplatelets, Chem. Mater. **23**, 3762 (2011).

[13] Q. D. Li, Q. L. Wei, W. B. Zuo, L. Huang, W. Luo, Q. Y. An, V. O. Pelenovich, L. Q. Mai, and Q. J. Zhang, Greigite Fe_3S_4 as a new anode material for high-performance sodium-ion batteries, Chem. Sci. **8**, 160 (2017).

[14] B. Zhang, G. A. de Wijs, and R. A. de Groot, Switchable fermi surface sheets in greigite, Phys. Rev. B **86**, 020406 (2012).

[15] Z. He, S. H. Yu, X. Zhou, X. Li, and J. Qu, Magnetic-field-induced phase-selective synthesis of ferrosulfide microrods by a hydrothermal process: Microstructure control and magnetic properties, Adv. Funct. Mater. **16**, 1105 (2006).

[16] H. B. Callen, The application of onsager's reciprocal relations to thermoelectric, thermomagnetic, and galvanomagnetic effects, Phys. Rev. **73**, 1349 (1948).

[17] H. B. Callen, A note on the adiabatic thermomagnetic effects, Phys. Rev. **85**, 16 (1952).

[18] V. Zlatić and R. Monnier, *Modern Theory of Thermoelectricity*, 1st ed. (Oxford University Press, New York, 2014).

[19] J. P. Wright, J. P. Attfield, and P. G. Radaelli, Charge ordered structure of magnetite Fe_3O_4 below the Verwey transition, Phys. Rev. B **66**, 214422 (2002).

[20] J. M. Lavine, Ordinary Hall effect in Fe_3O_4 and $(NiO)_{0.75}(FeO)_{0.25}(Fe_2O_3)$ at room temperature, Phys. Rev. **114**, 482 (1959).

[21] D. Reisinger, P. Majewski, M. Opel, L. Alff, and R. Gross, Hall effect, magnetization, and conductivity of Fe_3O_4 epitaxial thin films, Appl. Phys. Lett. **85**, 4980 (2004).

[22] P. Blaha, K. Schwarz, F. Tran, R. Laskowski, G. K. H. Madsen, and L. D. Marks, WIEN2k: An APW+lo program for calculating the properties of solids, J. Chem. Phys. **152**, 074101 (2020).

[23] J. P. Perdew, K. Burke, and M. Ernzerhof, Generalized Gradient Approximation Made Simple, Phys. Rev. Lett. **77**, 3865 (1996).

[24] V. I. Anisimov, I. V. Solovyev, M. A. Korotin, M. T. Czyżyk, and G. A. Sawatzky, Density-functional theory and NiO photoemission spectra, Phys. Rev. B **48**, 16929 (1993).

[25] G. K. H. Madsen and P. Novák, Charge order in magnetite. An LDA+U study, Europhys. Lett. **69**, 777 (2005).

[26] A. Roldan, D. Santos-Carballal, and N. H. de Leeuw, A comparative DFT study of the mechanical and electronic properties of greigite Fe_3S_4 and magnetite Fe_3O_4, J. Chem. Phys. **138**, 204712 (2013).

[27] A. J. Devey, R. Grau-Crespo, and N. H. de Leeuw, Electronic and magnetic structure of Fe_3S_4: GGA+U investigation, Phys. Rev. B **79**, 195126 (2009).

[28] S. Huang, D. Kang, X. Wu, J. Niu, and S. Qin, Pressure-induced structural and spin transitions of Fe_3S_4, Sci. Rep. **7**, 46334 (2017).

[29] R. F. W. Bader, *Atoms in Molecules: A Quantum Theory* (Oxford University Press, Oxford, 1990).

[30] G. K. H. Madsen and D. J. Singh, BoltzTraP. A code for calculating band-structure dependent quantities, Comput. Phys. Commun. **175**, 67 (2006).

[31] R. A. Matula, Electrical resistivity of copper, gold, palladium, and silver, J. Phys. Chem. Ref. Data **8**, 1147 (1979).

[32] W. R. G. Kemp, P. G. Klemens, and G. K. White, Thermal and electrical conductivities of iron, nickel, titanium, and zirconium at low temperatures, Aust. J. Phys. **9**, 180 (1956).

[33] J. S. Helman and B. Abeles, Tunneling of Spin-Polarized Electrons and Magnetoresistance in Granular Ni Films, Phys. Rev. Lett. **37**, 1429 (1976).

[34] L. Balcells, B. Martinez, F. Sandiumenge, and J. Fontcuberta, Magnetotransport properties of nanometric $La_{2/3}Sr_{1/3}MnO_3$ granular perovskites, J. Magn. Magn. Mater. **211**, 193 (2000).

[35] O. Kaman, Z. Jirák, J. Hejtmánek, A. Ndayishimiye, M. Prakasam, and G. Goglio, Tunneling magnetoresistance of hydrothermally sintered $La_{1-x}Sr_xMnO_3$-silica nanocomposites, J. Magn. Magn. Mater. **479**, 135 (2019).

[36] N. Furukawa, Y. Shimomura, T. Akimoto, and Y. Moritomo, Magnon scattering processes and low-temperature resistivity in CMR manganites, J. Magn. Magn. Mater. **226-230**, 782 (2001).

[37] Z. Jirák, O. Kaman, K. Knížek, P. Levinský, M. Míšek, P. Veverka, and J. Hejtmánek, High-field magnetoconductance in La-Sr manganites of FM and AFM ground states, J. Magn. Magn. Mater. **456**, 167 (2018).

[38] J. W. Koenitzer, P. H. Keesom, and J. M. Honig, Heat capacity of magnetite in the range 0.3 to 10 K, Phys. Rev. B **39**, 6231 (1989).

[39] B. Y. Pan, T. Y. Guan, X. C. Hong, S. Y. Zhou, X. Qiu, H. Zhang, and S. Y. Li, Specific heat and thermal conductivity of ferromagnetic magnons in yttrium iron garnet, Europhys. Lett. **103**, 37005 (2013).

[40] C. Kittel, *Quantum Theory of Solids*, 2nd revised printing (John Wiley and Sons, New York, 1987).

[41] S. R. Boona and J. P. Heremans, Magnon thermal mean free path in yttrium iron garnet, Phys. Rev. B **90**, 064421 (2014).

[42] G. N. Grannemann and L. Berger, Magnon-drag peltier effect in a Ni-Cu alloy, Phys. Rev. B **13**, 2072 (1976).

[43] S. M. Rezende and J. C. López Ortiz, Thermal properties of magnons in yttrium iron garnet at elevated magnetic fields, Phys. Rev. B **91**, 104416 (2015).

[44] R. Aragón, Magnetization and exchange in nonstoichiometric magnetite, Phys. Rev. B **46**, 5328 (1992).

[45] S. J. Watzman, R. A. Duine, Y. Tserkovnyak, S. R. Boona, H. Jin, A. Prakash, Y. Zheng, and J. P. Heremans, Magnon-drag thermopower and Nernst coefficient in Fe, Co, and Ni, Phys. Rev. B **94**, 144407 (2016).

[46] Z. Wang, J. E. Alaniz, W. Jang, J. E. Garay, and C. Dames, Thermal conductivity in nanocrystalline silicon: Importance of grain size and frequency dependent mean free path, Nano Lett. **11**, 2206 (2011).

[47] L. Yang and A. J. Minnich, Thermal transport in nanocrystalline Si and SiGe by *ab initio* based Monte Carlo simulation, Sci. Rep. **7**, 44254 (2017).

[48] S. M. Rezende, R. L. Rodríguez-Suárez, R. O. Cunha, A. R. Rodrigues, F. L. A. Machado, G. A. Fonseca Guerra, J. C. Lopez Ortiz, and A. Azevedo, Magnon spin-current theory for the longitudinal spin-Seebeck effect, Phys. Rev. B **89**, 014416 (2014).

[49] A. Miura, T. Kikkawa, R. Iguchi, K.-I. Uchida, E. Saitoh, and J. Shiomi, Probing length-scale separation of thermal and spin currents by nanostructuring YIG, Phys. Rev. Mater. **1**, 014601 (2017).

[50] M. Bailyn, Maximum variational principle for conduction problems in a magnetic field, and the theory of magnon drag, Phys. Rev. **126**, 2040 (1962).

[51] P. G. Klemens, Electrical conductivity of metals at low temperatures: Equilibrium between electrons and phonons, Proc. Phys. Soc. A **64**, 1030 (1951).

[52] J. M. Ziman, The thermoelectric power of the alkali metals at low temperatures, Philos. Mag. **4**, 371 (1959).

[53] C. Herring, Theory of the thermoelectric power of semiconductors, Phys. Rev. **96**, 1163 (1954).

[54] F. J. Blatt, M. Garber, and B. W. Scott, Thermoelectric power of dilute copper alloys. II, Phys. Rev. **136**, A729 (1964).

[55] F. J. Blatt, D. J. Flood, V. Rowe, P. A. Schroeder, and J. E. Cox, Magnon-Drag Thermopower in Iron, Phys. Rev. Lett. **18**, 395 (1967).

[56] Y. Tserkovnyak and M. Mecklenburg, Electron transport driven by nonequilibrium magnetic textures, Phys. Rev. B **77**, 134407 (2008).

[57] B. Flebus, R. A. Duine, and Y. Tserkovnyak, Landau-Lifshitz theory of the magnon-drag thermopower, Europhys. Lett. **115**, 57004 (2016).

[58] R. Ramos, M. H. Aguirre, A. Anadón, J. Blasco, I. Lucas, K. Uchida, P. A. Algarabel, L. Morellón, E. Saitoh, and M. R. Ibarra, Anomalous nernst effect of Fe_3O_4 single crystal, Phys. Rev. B **90**, 054422 (2014).

[59] N. Nagaosa, J. Sinova, S. Onoda, A. H. MacDonald, and N. P. Ong, Anomalous hall effect, Rev. Mod. Phys. **82**, 1539 (2010).

[60] Y. Shiomi, Y. Onose, and Y. Tokura, Extrinsic anomalous hall effect in charge and heat transport in pure iron, $Fe_{0.997}Si_{0.003}$, and $Fe_{0.97}Co_{0.03}$, Phys. Rev. B **79**, 100404(R) (2009).

[61] Y. Shiomi, Y. Onose, and Y. Tokura, Effect of scattering on intrinsic anomalous hall effect investigated by Lorenz ratio, Phys. Rev. B **81**, 054414 (2010).

[62] X. Li, L. Xu, L. Ding, J. Wang, M. Shen, X. Lu, Z. Zhu, and K. Behnia, Anomalous Nernst and Righi-Leduc Effects in Mn_3Sn: Berry Curvature and Entropy Flow, Phys. Rev. Lett. **119**, 056601 (2017).

[63] http://mgml.eu.

Correction: Errors in an in-line equation in the first sentence of the third-to-last paragraph of Sec. IV as well as in Eq. (A4b) and in-line equations appearing below it have been fixed.